WAGENINGEN
UNIVERSITY & RESEARCH

THE EFFECT OF WETLAND RESTORATION ON THE TIDAL HYDRODYNAMICS OF THE SCHELDT

Written by
Marit Schapendonk

19-04-2024
Supervised by
Joris Beemster and Ton Hoitink

Hydrology and Environmental
Hydraulics Group

Abstract

Estuarine regions have always been important for human settlements and economic activities due to abundant resources. Throughout history, mankind has been altering estuarine systems by dredging and wetlands reclamation, among other things, with little understanding of the effects on tidal hydrodynamics. This MSc thesis focuses on the Scheldt estuary and investigates the main processes that drive changes in tidal hydrodynamics after wetland restoration. For this purpose, data analysis of field measurements in the Scheldt and a numerical 1D model study were performed. The data analysis of pre- and post-restoration of the Hedwige-Prosperpolder showed no observable changes in tidal hydrodynamics. A numerical model was used to provide a more mechanistic insight into the impacts of wetland restoration on tidal hydrodynamics.

The model showed less pronounced effects on tidal hydrodynamics than previously predicted in other studies. The main process found is the establishment of a water level gradient along the channel towards the intertidal area, enhancing velocity seaward and decreasing the Mean High Water Level (MHWL), possibly due to the Bernoulli effect. Because of the increased velocity, friction in the channel also increases, which reduces the tidal range downstream as water movement slows. The tidal prism amplifies near the restored wetland. Still, it diminishes near the river mouth due to reduced tidal range, resulting in an overall decrease in tidal energy along the channel and a local increase in ebb dominance. Additionally, we found that wider intertidal areas (increased width along the river channel) at lower elevations further inland significantly influence the tidal hydrodynamics. This research highlights the impact of morphological characteristics of intertidal areas on tidal hydrodynamics and warrants further field investigations into the effect of tidal flats on tidal dynamics to provide better insights into the consequences of large-scale wetland restoration projects for future water management.

Contents

1 | Introduction

For centuries, humans have tended to move toward coastal regions, resulting in densely populated areas, particularly around estuaries (Neumann et al., 2015; Edmonds et al., 2017). The dynamic ecosystems and the significant economic importance are the driving factors of this migration (Meire et al., 2005; Giosan et al., 2014). Harbors for transportation, the fishing industry, fertile fluvisols for agriculture, diverse ecosystem services, and recent activities such as offshore mining and recreational use (Loucks, 2019; Nunn et al., 1999) increase the economic value of these regions. However, the pursuit of increasing economic benefits stimulated human interventions, such as dredging, hydropower dam installation, and land reclamation, altering estuarine systems globally (Wei et al., 2021; Blott et al., 2006).

These interventions enhanced economic gains but also had adverse effects on estuarine ecosystems, by for example, reducing intertidal habitat and influencing tidal hydrodynamics (e.g., tidal amplitude, tidal range, tidal intrusion, tidal prism, mean high water level (MHWL), mean low water level (MLWL), and phase differences) (Meire et al., 2005; Friedrichs and Aubrey, 1988). This change in tidal hydrodynamics could lead to increased flood risk in these areas (Edmonds et al., 2017), which is enhanced by climate-induced sea-level rise (Oppenheimer et al., 2019), and more frequently occurring storm surges (Lin et al., 2012; Bilskie et al., 2014).

An example of such an estuarine area is the Scheldt estuary, located in western Belgium and the Netherlands. In the Dutch part of the estuary, efforts were made to counteract these adverse effects of anthropogenic interventions in the past. This was done by reversing the land restoration of the Hedwige-Prosperpolder in 1907, among other restoration projects (Dauwe, 2019). In October 2022, the Hedwige-Prosperpolder, located next to the Western Scheldt, was opened (Figure 1.1), increasing intertidal area around the Scheldt, restoring an important habitat and giving the river more space to flow during high tide (NOS, 2022a, October 25). Restoring these wetlands is considered a nature-based solution as they act as adequate natural storm surge buffers by dissipating wave energy, storing floodwater, and growing with sea level rise (Temmerman et al., 2023).
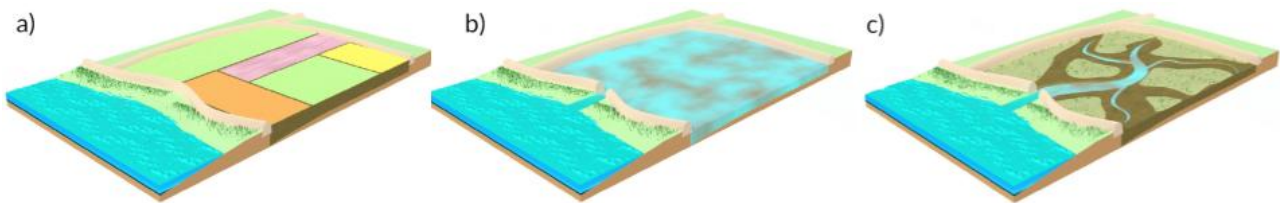

Figure 1.1: Picture A shows a drawing from the Hedwige-Prosperpolder from before the dike was breached and is still used for agriculture. Picture B shows the situation after the dike breach, and the water from the Scheldt can enter the intertidal area during the flood tide. Finally, Picture C shows the developed salt marsh ecosystem that can develop in the area in time. Adapted from Weisscher et al. (2022).

Understanding the dynamics of tidal waves within estuaries is crucial in restoration projects like the Hedwige-Prosperpolder. Research from Friedrichs and Aubrey (1994) showed that a wave that moves through a convergent estuary could be described with simple first and second-order solutions using the scaled momentum and continuity equations. This research shows that frictional damping reduces wave amplitude when a wave travels upstream through an estuary. However, bathymetric funneling (when the topography of the estuary funnels and concentrates the energy of waves) increases the wave's amplitude when it moves further upstream. Both processes, frictional damping, and bathymetric funneling, are important for describing how a tidal wave develops and deforms as it travels through an estuary (Friedrichs and Aubrey, 1994).

Moreover, studying tidal asymmetry, which describes the imbalance in the intention or duration of tidal ebb and flood currents within an estuary over a tidal cycle, adds more complexity to understanding the system. Generally, a shallow estuary exhibits a uniform and stable tidal asymmetry. The asymmetry of a wave in an estuary increases as it travels further upstream (Speer and Aubrey, 1985). Two processes balance the distortion of the tides in an estuary. The first process consists of the frictional distortion in the channels, while the second consists of the effect

of the change in size of the storage area in the intertidal flats. For the first process, shallow channels slow down the movement of low water more than that of high water, resulting in faster high water propagation and a longer ebb period. This effect contributes to a flood-dominant system. However, the second process reveals that when more storage area is added to the estuary, high water is delayed due to the diversion of floodwater over the intertidal area. During ebb tide, the water stays in the channel and is slowed down less than during high water, resulting in a longer flood period, indicating ebb dominance (Friedrichs and Aubrey, 1988). In summary, for an estuary without tidal flats, when a tidal wave enters the estuary, it develops a time asymmetry, generally resulting in flood dominance (longer falling tide and higher velocities during a flood). Conversely, when tidal flats are added to the estuary, the time asymmetry can lead to ebb dominance (more extended rising tides resulting in higher velocities during ebb). Thus, the interaction between shallowness and size of intertidal areas regulates the tidal distortion (Speer and Aubrey, 1985).

In addition to tidal asymmetry, other factors influence wave propagation in estuaries. Wave reflection, energy dissipation, and water exchange are important processes. Reflection of a wave can occur when an estuary is closed at the landward side, which is visible in the tidal signal as a standing wave if it is assumed that no friction occurs. A wave is also reflected at locations in the river where a change in channel depth or width occurs (van Rijn, 2011). Wave reflection could result in a local increase in the tidal range (Dronkers, 1964). The total energy flux, the amount of energy flowing through a given area per unit of time, in the system consists of potential and kinetic energy and is important as it helps to quantify the overall energy transfer within a fluid flow. Energy can be lost due to friction in an estuarine system. If a part of a tidal wave is reflected, less tidal energy travels upstream (Giese and Jay, 1989). When looking into energy dissipation in an estuarine system with tidal flats, Song et al. (2013) shows that tidal flats are important for storing tidal energy, primarily as potential tidal energy and with a minor component of kinetic tidal energy during flood tide. When the water is released from the tidal area during ebb, energy dissipation occurs by horizontal diffusion and bottom friction in the tidal flats, which is more significant than in the channels.

Weisscher et al. (2022) investigated the use of transitional intertidal areas along estuaries to reduce flood propagation and stimulate land-level rise. The findings indicate that when reclaiming wetlands alongside the Scheldt estuary, it is better to do this further upstream as you will have a stronger reduction of the mean tidal range than restoration at the river mouth. The authors also give a possible explanation for this. Namely, a polder located further upstream has a relatively larger gain in the intertidal area than adding the same polder near the mouth due to the convergence of the estuary. Therefore, the effect of increased friction caused by the extra width is greater for a polder further upstream. Additionally, because opening a polder can lead to flood dominance, it transports more sediments into the estuary, making the channels shallower and increasing friction on longer time scales, which dampens the tides.

Stark et al. (2017) observed comparable results in their experiments. Furthermore, they also found, using a two-dimensional depth-averaged hydrodynamic model, that the volume and location of the intertidal wetland area significantly influence the tidal hydrodynamics of the Western Scheldt estuary. The research shows changes are different when the intertidal storage area is near the main channel compared to the side basin. When the tidal flats affect the channel's cross-section and create friction, it affects the tidal asymmetry; flood-dominance is amplified when the tidal flat is lower than sea level, and ebb-dominance is increased when tidal flats are around mean sea level or slightly above. The location of the intertidal area affects the tidal prism along the estuary. There will be an increase downstream of the area and a decrease upstream. Furthermore, a decrease in the tidal range seaward of the setback was predicted (Stark et al., 2017).

The Dutch government plans to create more intertidal areas to increase biodiversity. Generally, these intertidal areas are relatively small and can affect tidal hydrodynamics locally and on a larger scale (Stark et al., 2017). Stark et al. (2017) shows that the local and regional influence depends on the volume of the intertidal area and its distance from the river mouth. It is difficult to understand the underlying physical processes affecting tidal hydrodynamics. Mainly because, on the one hand, the added intertidal area can enhance the tides as more water can be stored in the intertidal area during floods, which increases the tidal prism. On the other hand, the tides could also be weakened because of the increased frictional forces by flow through shallow channels and the added storage area.

Therefore, estimating how much transmission and reflection of tidal energy will occur after the increase in

intertidal area is not straightforward. The transmission and reflection of tidal energy can depend on the geometrical properties of the estuary, the mean sea level, tidal amplitude, and phase. Besides, it is unclear what processes influence the changes in tidal prism along the channel after wetland restoration. These aspects will be explored further in this study. Also, it is unclear if the findings of Stark et al. (2017) can be applied to other estuarine systems and if the predicted effects for the Scheldt estuary are as large in real life.

The goal of this master's thesis study is to offer a mechanistic understanding of the effects of the construction of a local intertidal area on tidal hydrodynamics. First, I analyze data gathered around the time of the opening of the Hedwige-Prosperpolder to investigate if the results found by Stark et al. (2017) for tidal amplification, phase difference, and tidal asymmetry can also be measured in the field. Thereafter, I will use an idealized numerical 1D model to replicate the results from Stark et al. (2017). Subsequently, I investigate how the tidal prism at the estuary and tidal energy transmission and reflection depend on the geometric characteristics of both the estuary and the intertidal area to be developed.

1.1 Research objective and questions

The research objective of this master thesis is to gain more insight into the changes in tidal hydrodynamics, which in this study consists of tidal amplitude, tidal range, tidal intrusion, tidal prism, MHWL, MLWL, and the phase difference. These tidal hydrodynamics are likely to change after wetland restoration, also known as an increase in intertidal area. An example is the Hedwige-Prosperpolder, which was opened in 2022 and introduced in the problem description. Besides that, an attempt will be made to understand the fundamental mechanisms that result in such changes in tidal hydrodynamics after wetland restoration. To achieve this objective, this master thesis will address the following main research question and the sub-research questions:

Main research question: *What processes explain the changes in tidal hydrodynamics of the Western Scheldt after wetland restoration?*

Sub-research questions:
- Which changes in the tidal hydrodynamics can be observed after the opening of the Hedwige-Prosperpolder?
- Do the observed changes in tidal hydrodynamics following the opening of the Hedwige-Prosperpolder correspond with the results reported by Stark et al. (2017)?
- How do the energy dissipation, water exchange, and tidal asymmetry in the system change when an intertidal area is opened at different locations, elevations, and for different shapes, and does this influence the tidal hydrodynamics?
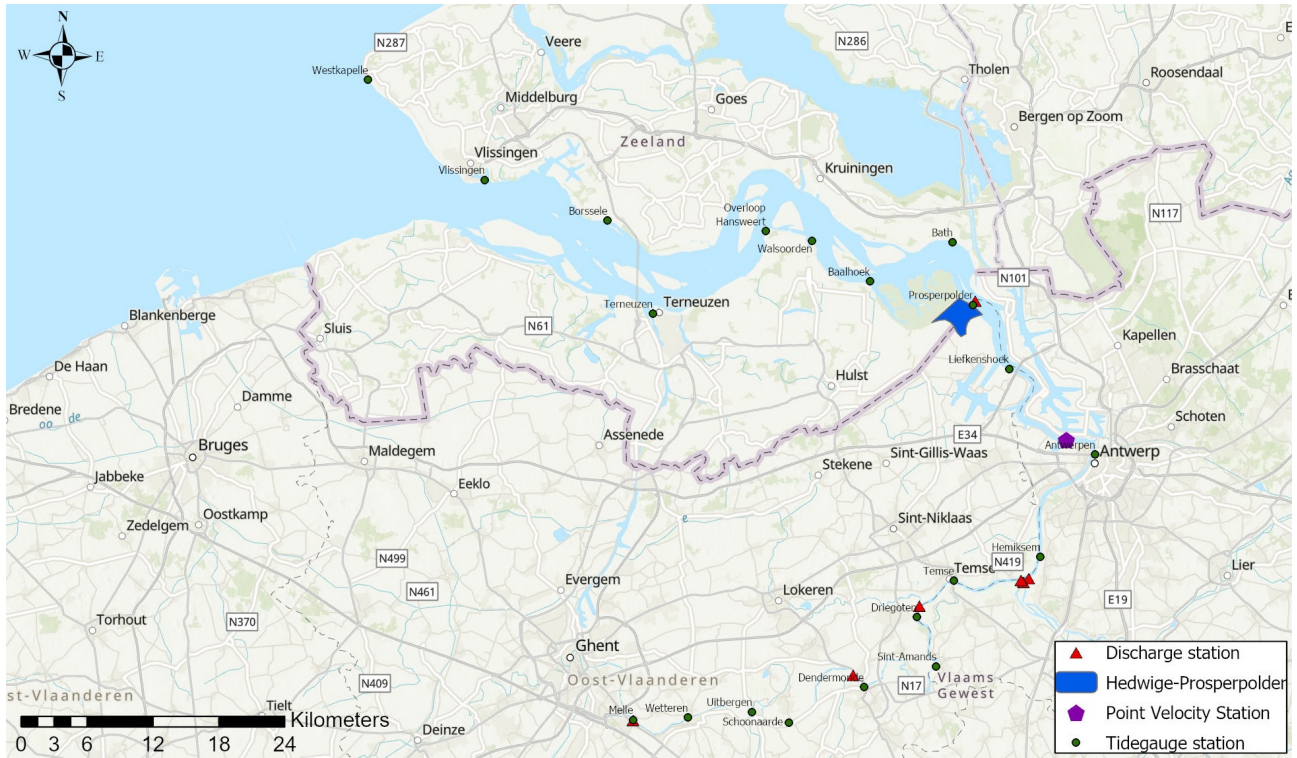
2 | Field site

2.1 The Scheldt estuary

Figure 2.1: A map of the study area, showing the Scheldt estuary and the location of the Hedwige-Prosperpolder, together with the locations of the water level and discharge measurement stations used. The names of the tide gauge stations are also included in the map.

The field site of this study comprises the estuary of the river Scheldt, located in the southwest of the Netherlands and the northwest of Belgium (Figure 2.1). The Western Scheldt is part of the estuary located in the Netherlands. This part of the Scheldt has a complicated hydraulic regime with many channels, mudflats, and salt marshes. The part of the estuary in Belgium is named the Sea Scheldt. The tides influence the estuarine part of the river as it flows into the North Sea at Vlissingen. The tidal influence can be measured up until the weir at Gentbrugge, 160 km from the mouth. The part of the river called the Sea Scheldt is less wide than the Western Scheldt and has a more regular morphology; the estuary converges from a 5 km width at Vlissingen to a width of only 50 m near Gent. The order of the convergence length scale is Lb=25 km (Van Rijn et al., 2010). When passing Gent, the remaining part of the river has been largely canalized, and the river flows for another 190 km until the source near St. Quentin in France (Claessens et al.; Stark et al., 2017). For this study, the focus will be on the tidal Scheldt, starting at the mouth near Vlissingen and continuing to the sluice gate at Gentbrugge in Belgium.

2.1.1 Hydrodynamics and morphology of the Scheldt

The estuarine part of the river Scheldt exhibits a semi-diurnal tide with a meso- to macro-tidal regime (Wang et al., 1999). Generally, the tidal range in an estuary is affected by four processes: 1) inertia related to acceleration and deceleration effects, 2) amplification due to convergence land inwards, 3) damping due to bottom friction, and 4) reflection (partially) at abrupt changes in the cross-section of the river (Van Rijn et al., 2010). For the Scheldt, the mean tidal range changes from 4 m at the mouth near Vlissingen to 5.2 m near Antwerp in the Sea Scheldt. This increase in tidal range is mainly caused by the funneling bathymetric characteristics of the estuary and the decreasing

depth, but could also result from reflections of the tidal wave. Moving further inland towards Gent, the tidal range decreases again due to shoaling and the resulting frictional damping (Wang et al., 1999).

The Dutch part of the estuary is well-mixed despite a mean river outflow of approximately 120 m^3/s, which is relatively small compared to the tidal prism of the river of about $2 \cdot 10^9 \ m^3$ during one tidal cycle (Wang et al., 1999). The peak tidal discharge during flood is around 30% larger than the peak tidal discharge during ebb. The propagation speed of the tidal wave (mean of LW and HW) varies between 15 m/s at the mouth and 11 m/s at the landward end of the estuary near Bath (Van Rijn et al., 2010). Before the opening of the Hewige-Prosperpolder, a phase difference of about 2.5 hours (72°) between the vertical and horizontal tide was observable, indicating that the tidal wave is neither completely standing nor progressive (a standing wave describes a wave that is stationary and does not propagate through a medium whereas a progressive wave does) (Van Rijn et al., 2010; Wang et al., 2002; Stark et al., 2017).

When considering wave reflection, the study from Van Rijn et al. (2010) discovered that part of the incoming tidal wave may be reflected near Bath because the river bends at this location. After the wave is reflected, it will propagate towards the North Sea and slowly dampen out due to the increased channel width. It will not be noticeable anymore at the mouth. Additionally, a pronounced variation in width at the entrance of the estuary and between Bath and Antwerp is visible. Because of the large amplification in the tidal range between Bath and Antwerp, Van Rijn et al. (2010) suggests wave reflection may occur of the order of 0.5 to 1 m near Bath.

Regarding the morphology, the estuary is funnel-shaped, with different channels exhibiting a repetitive pattern when moving upstream from the river mouth. This pattern consists of a straight flood channel and a meandering ebb channel. These channels are linked by smaller channels and separated by tidal flats in a large part of the estuary. The riverbed predominantly consists of fine to medium sand with a diameter of approximately 200-300 μm, as the depth average flow velocity in the channels is around 1.5 m/s, resulting in mainly suspended load sediment transport through the channel (Wang et al., 1999).

2.1.2 Tidal asymmetry

General introduction to tidal asymmetry

Tidal asymmetry is the deformation of a tidal wave and occurs in tidal estuaries and lagoons. Namely, when a wave enters an estuary, its amplitude, shape, and speed can change, deforming the wave as it propagates further inland (Guo et al., 2019). It is important to understand the role of tidal asymmetry because of its controlling role on residual sediment transport and the large-scale morphological evolution (Dronkers, 1986). Both statistical and harmonic methods effectively indicate if tidal asymmetry occurs (Guo et al., 2019).

When tides from the ocean enter the estuary, non-linear effects occur due to changes in bathymetry (topography of the riverbed). These interactions generate high-frequency harmonic constituents of the ocean tides (high-frequency harmonic constituents are additional tidal components with higher frequencies than the principal tidal constituents M2 and S2). These constituents grow and increase the tidal asymmetry (Friedrichs and Aubrey, 1988). There are two types of tidal asymmetry. Firstly, vertical tidal asymmetry indicates the tidal asymmetry in the water levels; secondly, horizontal tidal asymmetry refers to the flow velocity. Both types are influenced by shallow water effects (Guo et al., 2019).

M2 is the primary tidal constituent used in tidal analysis, also known as the principal lunar semi-diurnal tide, with a period of 12 hours and 25 minutes, which is the time it takes the moon to complete an orbit around the Earth. M4 is a higher-order harmonic of M2 and is significant in estuaries where shallow water effects occur (Parker, 2007). Vertical asymmetry occurs when the flood period is not equal to the ebb period. Flood dominance occurs when the time it takes for the water level to rise is shorter than the time it takes to fall. Ebb-dominance occurs if the opposite is true (Figure 2.2). The ratio of the amplitude of the semi-diurnal tide (M2) and the overtides (M4, M6, etc.) can determine the strength of vertical tidal asymmetry. The nature of asymmetry is determined by the phase difference between tidal constituents M4 and M2, which is considered representative of phase differences between other quarter and semi-diurnal constituents as well (Speer and Aubrey, 1985; Wang et al., 1999). For the vertical
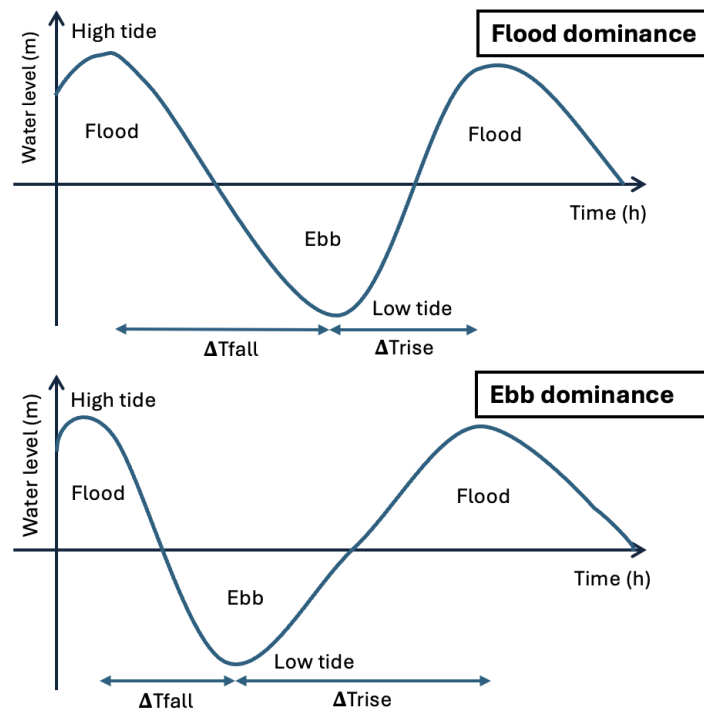
Figure 2.2: An example of flood and ebb dominance for vertical asymmetry in a system. Flood dominance occurs when the duration of the rise of the tides is shorter than the fall of the tides ($\Delta T_{rise} < \Delta T_{fall}$). Ebb dominance occurs when the duration of the rise of the tides is greater than the fall of the tides ($\Delta T_{rise} > \Delta T_{fall}$).

tide, a phase difference between 0° and 180° shows flood dominance, and a phase difference between -180° and 0° shows ebb-dominance (Wang et al., 1999, 2002).

Horizontal asymmetry has two sub-types: the difference between the ebb and flood velocities and the difference in duration of slack water for high and low water (Bolle et al., 2010). Only the difference in flood and ebb velocity will be considered for this study. Horizontal asymmetry is considered ebb-dominant, with greater velocities during ebb, for a phase difference between -180° and -90° or 90° and 180°. Ebb dominance is considered greatest for a phase difference of 180°. Greater velocities during flood, implying flood dominance, occur for a phase difference between -90° and 90° (Stark et al., 2017). Generally, asymmetry in the vertical tide will cause an asymmetry in the horizontal tide, and the relationship between the two is non-linear (Bolle et al., 2010).

Tidal asymmetry in the Western Scheldt

When looking into the tidal asymmetry of the Western Scheldt, Wang et al. (1999) found that three mechanisms may induce residual flows, which can interact with tidal currents to amplify asymmetries. Firstly, non-linear friction can result in bathymetry-related circulations. An example of topography-induced residual flow is the flood-dominated residual flow in wetlands. Secondly, residual flows can occur due to horizontal geometry originating from inertial effects and non-linear friction. Thirdly, the Coriolis force can induce residual flows as well. However, they found that bathymetry-related circulations are most important for creating residual flows for the Western Scheldt. Long-term current observations showed how, at the location of the ebb channel, ebb-dominated flow prevails, and in the flood channel, a relatively large residual flood flow occurs. Furthermore, the non-linear interactions are stronger during spring tide than during neap tide, so the asymmetry in the horizontal and vertical tide is greater during spring tide.

Wang et al. (1999) also showed that the relationship between vertical and horizontal asymmetry is non-linear because cross-sectional area and storage width change with the water level, called the hypsometry effect. This means that in the case of flood-dominant vertical asymmetry, there is not necessarily flood-dominant horizontal asymmetry.

For the Western Scheldt, they found that the phase difference between M4 and M2 is small. Therefore, the asymmetry in the discharge is increased by the hypsometric properties of the channel, and the asymmetry in the flow velocity is weakened.

Previous studies by Speer and Aubrey (1985), Dronkers (1986), Friedrichs and Aubrey (1994), and Friedrichs and Aubrey (1988) found that the mean channel depth and intertidal area strongly influence vertical tidal asymmetry. Deep estuaries with large intertidal areas are ebb-dominant, whereas shallow estuaries tend to be flood-dominant. Wang et al. (1999) found that for the Western Scheldt, this applies as well, with flood dominance in parts of the Scheldt with larger water depths and intertidal areas compared to parts of the channel where ebb-dominance prevails. Bolle et al. (2010) and Wang et al. (1999) also found that anthropogenic changes to the system influence the tidal asymmetry of the Western Scheldt. Dredging of the western Scheldt in the past resulted in less flood-dominance of the vertical tide in the landward part of the estuary. In the seaward part of the estuary, the increase in intertidal area resulted in more flood-dominance.

2.2 Wetland restoration in the Scheldt

In the past, the estuary had more intertidal areas. Between 1650 and 1968, people began embanking former intertidal regions, reducing the tidal flat size by 44%. As a result, the water storage area during high water levels decreased. Currently, only 9000 hectares of intertidal wetlands remain in this area (Van der Spek, 1997). The largest intertidal area around the estuary is the Verdronken land van Saeftinghe, which has an area of 3500 ha and is one of Europe's most extensive and essential saltmarshes (Dauwe, 2019).

Saeftinghe used to be an area surrounded by dikes since the fourteenth century when the first settlers used the higher area for agriculture. Storm surges repeatedly broke the dikes in the past, and part of the hinterland disappeared again under the waves. Major floods took place in 1570 and 1574. Later, during the Eighty Years' War, the dikes were broken in an attempt to prevent the Spanish armies from conquering the city of Antwerp, and the land was flooded again, resulting in the natural area we know today (Zeeuws Landschap, n.d.). During the time in which more intertidal areas were embanked, the tidal prism decreased by less than ten percent, which is surprising considering the large decrease in the intertidal areas over the years (Van der Spek, 1997). A significant increase in the tidal range is visible compared to before the wetland restoration started due to changes in bathymetry and the North Sea forcing. Additionally, an increased penetration of the tidal wave and a more considerable speed for the wave propagation is also visible (Van der Spek, 1997; Coen et al., 2008).

2.2.1 The Hedwige-Prosperpolder project

In 2005, it was decided in the Scheldt treaties to give the Scheldt more space to flow to prevent flooding during a storm surge and to restore tidal ecosystems (Dauwe, 2019). Tidal ecosystems develop when an area is largely dry during ebb tide and covered by salt or brackish water during flood tide. Because of the tides, sand and silt keep being displaced and, in time, form salt marshes and mudflats, which are important habitat types for certain species like mollusks and worms. Creating these habitats increases biodiversity in the area (Keith et al., 2020; Dauwe, 2019). Despite opposition in Dutch politics and corresponding delays, it has been agreed that the embanked land, now forming the Hedwige-Prosperpolder, would be given back to the Scheldt by breaching the dikes (Figure 2.4) (NOS, 2022, June 7). This measure would create 465 ha of additional intertidal area (Dauwe, 2019). On the 25th of October in 2022, the first water flowed via a creek into the Hedwige-Prosperpolder (Figure 2.3) (NOS, 2022a, October 25). The Hedwige-Prosper project is part of a larger Sigma plan in Vlaanderen, which aims to reduce the risk of flooding in Belgium, and part of the Natuurpakket Westerschelde in the Netherlands (Dauwe, 2019).

(a) A top view of the Hedwige-Prosperpolder after the opening in October 2022 during ebb tide. People dug several creeks to promote the area's natural development. Retrieved from Scheyen (2023, 25 mei).

(b) A top view of the Hedwige-Prosperpolder after the opening in October 2022 during flood tide. In the bottom left, the construction of a panorama hill for tourism is visible. Retrieved from Dauwe (2019).

Figure 2.3: A top view of the Hedwige-Prosperpolder after the opening in October 2022 during ebb and flood tide.
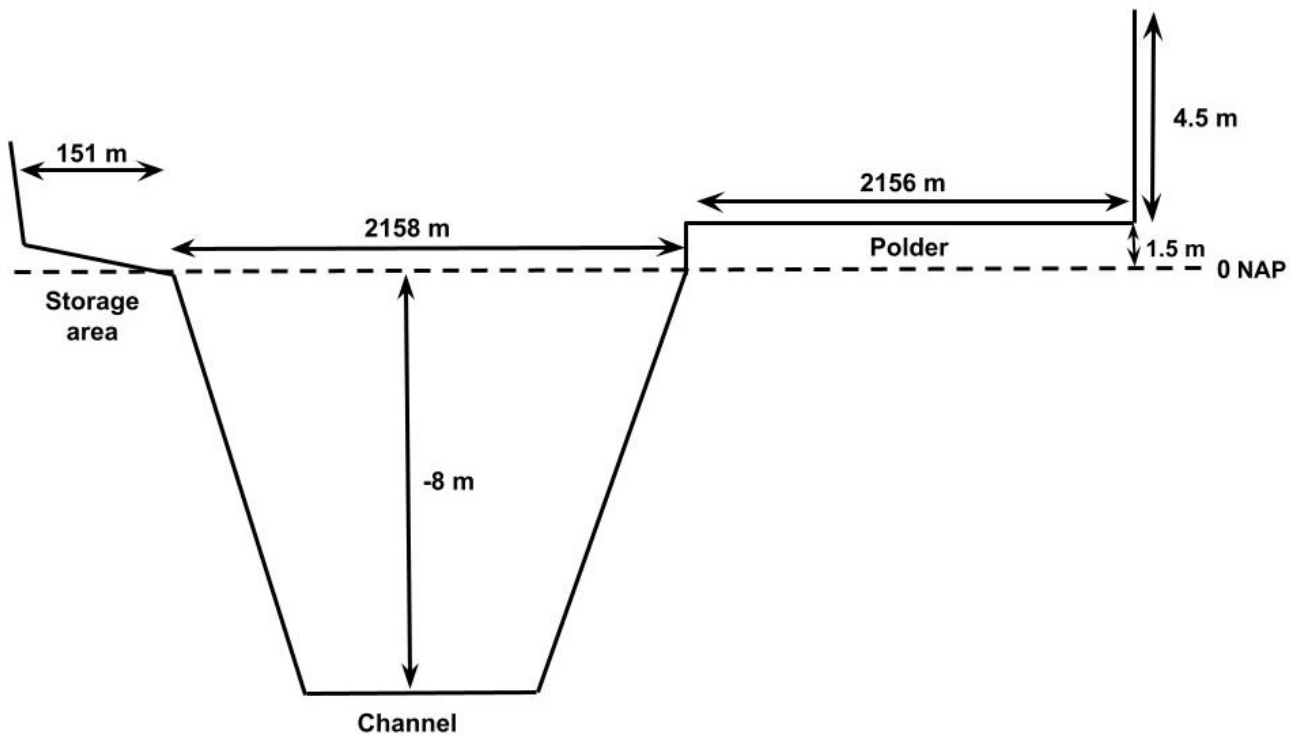

Figure 2.4: A simplified schematic cross-section of the river Scheldt and the Hedwigeprosper polder located next to the river with average depth and width values. Displayed values retrieved from Ahn (2023).

3 | Methods

The methods can be divided into two parts. The first part of the methodology consists of data analysis on the effect of the opening of the Hedwige-Prosperpolder on the tidal hydrodynamics in the data analysis and the model study results, velocity, and discharge data measured in the Scheldt during the year before the opening of the Hedwige-Prosperpolder and for the year after were considered. I used this data to investigate if changes in tidal hydrodynamics can be observed after wetland restoration in the field. For the second part of the methodology, I performed a model study using and adjusting a 1D numerical model to investigate which processes are most important in understanding how tidal hydrodynamics change after wetland restoration. Combining the results of both the data analysis and the model study helped to create a better mechanistic understanding of the effects of constructing an intertidal area in the Scheldt.

3.1 Data Analysis

For the data analysis, the water level, velocity, and discharge data measured at several stations in the Scheldt were used to investigate if changes in tidal hydrodynamics can be observed after wetland restoration in the field. I first collected the data from online sources for this part of the investigation. After that, I used linear interpolation to fill the gaps in the data I retrieved, after which I investigated the change in tidal hydrodynamics due to a change in the intertidal area.

3.1.1 Data collection

First, I gathered water level data in meters for 20 stations along the main branch of the river Scheldt for the data range spanning from the 25th of October 2021 until the 25th of October 2023 (Figure 2.1). This period contains one year of data before the opening of the Hedwige-Prosperpolder (25-10-2021 to 25-10-2022), which will from now on be referred to as the year 2022 and for the year after the opening of the Hedwige-Prosperpolder (25-10-2022 to 25-10-2023), which from now on will be referred to as the year 2023. I retrieved the water level data measured at the stations in Belgium from Waterinfo (n.d.), a website owned by the Belgian government, containing measurements from Flanders Hydraulics (MOW-HIC). For the Dutch measurement stations, I retrieved the water level data from Rijkswaterstaat (n.d.), a website the Dutch government runs to make water level data available for public use.

For the data analysis, I only considered stations located along the Scheldt between the river mouth and the city Gent, as a tidal wave can not propagate further upstream due to the weir located in this city. The following demands were set to work with consistent data without large gaps. 1) The measurement station should have high-resolution measurements, meaning that the water level was measured at least every 10 minutes, 2) a station should have sufficient data quality, missing less than 5% of the data in the time frame considered; and 3) when Rijkswaterstaat and the Belgian government measured at the same location, I only used the measurements from the country where the measurement station was located. Generally, there were only small gaps in the data of a few hours, but for two stations (Overloop van Hansweert and Walsoorden), data is lacking for September 2023. Furthermore, for station Schaar van de Noord, 9.5% of data is missing and is therefore not used in this data analysis. The closest water level measurement station from the Hedwige-Prosperpolder is Belgium's "Prosperpolder" measurement station, located around 780 m upstream from the nearest opening of the Hedwige-Prosperpolder to the Scheldt (Figure 2.1). This station contained sufficient data for the period considered. Additionally, this was an important measurement station to include in the data analysis as it was assumed that it could most accurately show what happens to the tidal dynamics after the opening near the polder, as it was expected that visible changes would be largest here.

Secondly, I also gathered velocity measurements in meters per second for the data range from one measurement station called Oosterweel-Boven SF/Zeeschelde, located near Antwerp (Figure 2.1) from Waterinfo (n.d.). At this location, point-velocity measurements were made, and the direction of the velocity in degrees was measured every five minutes. The data for this station has a few gaps of a few days during the time period considered, but the

missing data gaps were small enough to still use the data. However, another measurement station closer to the Hedwige-Prosperpolder could also capture point velocity measurements. Unfortunately, this dataset was excluded due to insufficient data availability during a critical period starting on the 1st of October 2022 and spanning the entire year of 2023.

Finally, I collected discharge data, measured every five minutes from a measurement station in Belgium next to Melle (Figure 2.1). I retrieved the data for the data range from Waterinfo (n.d.). Calculated discharge measurements at the border between Belgium and the Netherlands were also available but not for 2023 and, therefore, excluded from the research.

3.1.2 Interpolation of the data

After the data collection, I first interpolated the water level data because some of the measurement stations along the Scheldt had gaps in the data for the considered range. For interpolating the water level data, I started with a classical harmonic tidal analysis performed for the water level data of all measurement stations along the channel using the package T-tide in MATLAB from Pawlowicz et al. (2002). I also used T-tide to perform nodal corrections to account for some of the unresolved constituents. After performing the classical harmonic tidal analysis, the tidal behavior per station was predicted for the time frame in which the water level data were available. I subtracted the tidal prediction from the original measured data per time-step for each station to interpolate the data. I filled the gaps in the resulting time series of the difference with linear interpolation. After that, I added the tidal prediction to the interpolated time series of the tidal residual (difference between the original data and the predicted data) per station to create the new interpolated water level time series for all stations.

For the interpolation of the point velocity measurements, I first used the direction of the velocity (θ) and the magnitude of the velocity ($V_{magnitude}$) to calculate the streamwise velocity component (V_y) in the direction of the channel length and the transverse velocity (V_x) in the direction perpendicular to the channel length for every time step using equations:

$$V_y = V_{magnitude} \cdot sin(\theta) \tag{3.1}$$

$$V_x = V_{magnitude} \cdot cos(\theta) \tag{3.2}$$

After that, I performed a classic harmonic tidal analysis with T-tide from Pawlowicz et al. (2002), using both V_x and V_y as complex input. I also used T-tide to perform nodal corrections to account for some of the unresolved constituents. Following that, I subtracted the tidal prediction, given by the harmonic analysis, from the observed data per time-step for each station. Subsequently, I performed linear interpolation for the gaps in the data series of the tidal residual. I again added the predicted time series to the interpolated tidal residual to find the interpolated time series of the original data per station.

3.1.3 Investigation of the tidal hydrodynamics

Water level data

To answer the first and second sub-research questions, I investigated the tidal hydrodynamics, including tidal amplitude, tidal range, tidal intrusion, MHWL, MLWL, and phase difference, for 2022 and 2023 to investigate if changes in these tidal characteristics were visible due to the opening of the intertidal area. First, I used a classical harmonic analysis using T-tide to investigate the significant constituents of the tidal signal in the Western Scheldt. After that, the average phase and amplitude for M2, M4 and M6 were considered.

I mainly focused in this investigation and during my following model study on the M2, M4, and M6 tidal constituents because the M4 overtides originate from the nonlinear terms in the continuity and moment equation (bottom friction and advective inertia term), and the phase difference described by $2\phi_{M2} - \phi_{M4}$ is representative of other phase differences between other semi-diurnal and quarter diurnal species (Wang et al., 1999; Speer and Aubrey, 1985). Analyzing this phase difference showed the nature of the asymmetry of the tides. However, because, in reality, the tidal asymmetry is also influenced by M6 overtides, which are induced by interactions between M2 and

M4 constituents but not by M6 on its own, the M6 tidal constituent was also considered in the investigation (Parker, 1984).

Additionally, I used the interpolated water level data for the different stations to calculate the change in mean high water level and mean low water level for every station along the Scheldt for 2022 and 2023. Furthermore, I calculated the average high water phase difference by calculating how much time it takes on average for a high water peak to travel from the station at the mouth (Westkapelle) to each station along the river. I calculated the average travel time per station of both 2022 and 2023 and investigated the change in phase difference between the two consecutive years for each station. I did the same for the mean low water phase difference by calculating the average time it took the low water valley to travel from the mouth to each station per year. Moreover, I calculated the average tidal range for each station for the year before the opening of the intertidal area (2022) and for the year after (2023). The tidal range is defined as the difference between consecutive high and low water levels.

Moreover, I compared the vertical tidal asymmetry of the Western Scheldt before and after the opening of the intertidal area based on the duration of the rising and falling tides. For each station, the average time it takes for the tides to rise and fall is calculated per station for 2022 and 2023. When the average time it takes for tides to fall is longer than for tides to rise, it results in a flood-dominant system. When it is the other way around, it points towards an ebb-dominated system (Stark et al., 2017).

After making a comparison of the tidal hydrodynamics in 2022 and 2023, I also retrieved water level data for all stations used before, except Borselle, Prosperpolder, Uitbergen, and Driegoten for the eleven years ranging between 1/1/2010 00:00 and 1/1/2021 00:00 (for the stations Borselle, Prosperpolder, Uitbergen, and Driegoten, data was not available during this time or had gaps in the time frame larger than 6 months). After that, I calculated the same components of the tidal hydrodynamics, tidal range, MHWL, and MLWL, R_t, the phase difference between high water, and the phase difference between low water. Next, I calculated the percentual difference for consecutive years for each parameter along the channel to gain some perspective of changes in these parameters over the years due to changes in tidal forcing, weather, and river discharge.

Point velocity data

To analyze the velocity data, the average ebb and flood velocity were calculated for both years. Moreover, I performed a harmonic analysis using complex input of the point velocity data V_x and V_y for 2022 and 2023. After making the tidal prediction for both years, I compared the amplitude and phase of M2, M4, and M6 tidal constituents to the harmonic analysis results using water level data at that location. After that, I researched the differences in horizontal tidal asymmetry, using the M2, M4, and M6 tidal constituents for the year before the opening of the Hedwige-Prosperpolder and the year after.

To be able to put the observed changes in average ebb and flood velocity and horizontal tidal asymmetry between 2022 and 2023 in perspective, the same analysis for the point velocity data measured near Antwerp was done for the data range 01/01/2010 00:00:00 until 01/01/2016 00:00:00. This data range consists of velocity measurements taken every ten minutes for six consecutive years, and was chosen because no major dredging activities occurred during this time in the Scheldt (H. Heusinkveld, personal communication, April 5, 2024) and because the data contains little gaps. After performing the tidal harmonic analysis for each year, the percentual difference in average maximum flood velocity and average maximum ebb velocity ($\bar{V}$) was calculated between consecutive years (n) with:

$$\bar{V} = (V_n - V_{n-1})/V_{n-1} * 100\% \tag{3.3}$$

3.2 Model study

For the model study, I imposed the Scheldt's bathymetry in a one-dimensional hydrodynamic model. Then, I calibrated the model by changing the boundary conditions and the Chézy coefficient. I also imposed a tidal wave at the river mouth, consisting of M2, M4, and M6 tidal constituents. After optimizing the model performance, I implemented

multiple intertidal areas at different locations of different widths and elevations to investigate their effect on the river's hydrodynamics and identify the important processes that resulted in these changes.

3.2.1 Model description

This research relied on a 1D finite difference numerical model of an idealized estuary built in Matlab (J. Beemster, personal communication, November 20, 2023). A 1D model was preferred over a more complex 2D or 3D model of the Scheldt for this investigation, as a 1D model was easier to calibrate and also suitable for studying flow along a channel. Furthermore, the running time of a 1D model was much shorter due to lower computational demands. Because this study mainly focuses on large-scale hydrodynamics, a 2D or 3D model, which provides a more accurate representation of frictional losses on the intertidal platform and a better description of transverse flows, was unnecessary. A 1D model was also chosen because it only includes the most relevant processes, like tidal flushing, changes in energy, and reflection of tidal waves. This made it more straightforward to study the responses of tidal hydrodynamics across many parameter values, and interpreting these was considered easier because the amount of complex nonlinear feedbacks was minimized (Hoitink et al., 2020).

The model described a single river channel consisting of the imposed bathymetry of the Scheldt that converges and decreases in depth when moving further inland (Figure 3.2). Furthermore, the one-dimensional shallow water equations, consisting of the momentum and continuity equations, were implemented.

$$\frac{\partial b_c \zeta}{\partial t} + \frac{\partial Q}{\partial s} + q_s = 0 \tag{3.4}$$

The continuity equation (Equation 3.4), which describes the conservation of mass, where b_c describes the channel width (m), ζ shows the tidal elevation (m), Q is the discharge (m^3/s), s shows the distance (m), and $q_s = \frac{\partial b_s \zeta}{\partial t}$, with b_s the storage width (m), which shows the transportation of water from the main channel (part of the river that also contains water during ebb tide) into the intertidal area per channel length.

$$\frac{\partial Q}{\partial t} + \frac{\partial}{\partial s}\frac{Q^2}{A_c} + \frac{Q}{A_c}q_s = -gA_c\frac{\partial \zeta}{\partial s} - \frac{g}{C^2}\frac{Q|Q|}{A_c d} \tag{3.5}$$

The momentum equation (Equation 3.5), consists of A_c which is equal to the channel cross-sectional area (m^2), g stands for the gravitational acceleration of 9.81 m/s^2, d is the depth (m), and C is the Chézy coefficient $(m^{0.5}/s)$. These two equations convey water storage within the secondary basins and the storage on the intertidal platform with a storage term in the mass equation and a momentum loss term in the momentum equation (Dronkers, 1964).

The model used a staggered grid spatial scheme and calculated the water level elevation for odd grid points and the discharge for even grid points. A central differencing scheme was used for all spatial derivatives, and an upwind differencing scheme was used for the advective and lateral momentum exchange terms. A leapfrog scheme was used to solve the temporal derivatives. In the model, the water elevation was first renewed using the continuity equation and an Euler forward method, after which the new geometry and discharge were calculated. This is called the semi-implicit method (Battjes and Labeur, 2017).

3.2.2 Implementation of the bathymetric data of the Scheldt into the model

To make the one-dimensional model used for this research representative of the Scheldt, I imposed the bathymetry of the river. To include the bathymetry of the Scheldt in the model, I first loaded a GIS file with depth data for the Scheldt into Matlab with a grid cell surface of 25 m^2 (J. Beemster, personal communication, November 20, 2023). According to Rijkswaterstaat, the Western Scheldt is between -51.44 and -13.44 m deep (van Infrastructuur en Waterstaat, 2022, 27 december), and no large hills occur in the area according to Ahn (2023). Therefore, outliers smaller than -60 m and greater than 30 m were deemed non-representative for the river. These values were replaced through linear interpolation, taking into account adjacent depth values. Almost 2 million depth measurements of the Scheldt were available in the bathymetric data, of which 3419 (0.02 %) were smaller than -60 m, and 5010 (0.03 %) were greater than 30 m.
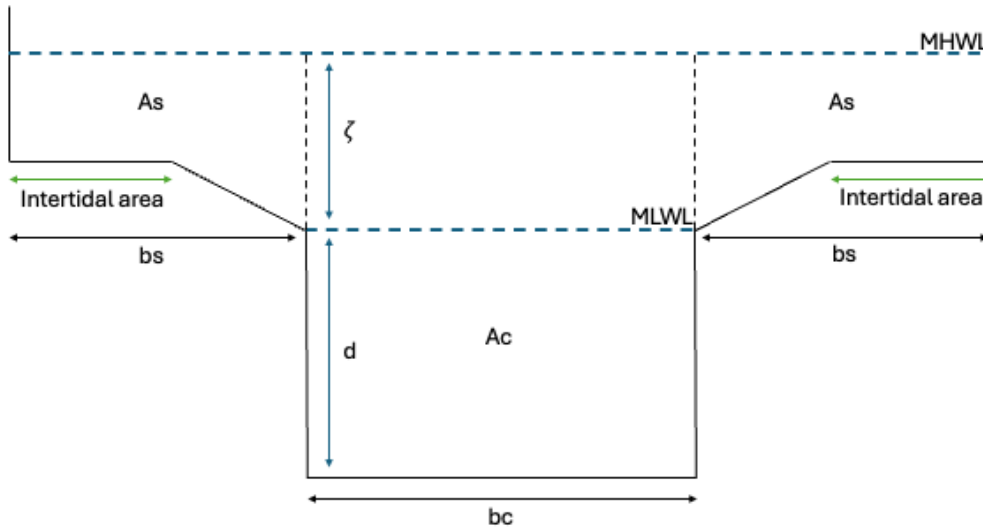
Figure 3.1: A schematic overview of the cross-section of the river Scheldt at the location where a polder is implemented. This is how it is built into the model with the intertidal area on either side of the channel. As is the storage flow surface area, and Ac is the channel flow surface area. d is the depth of the channel, and ζ is the tidal elevation. bs is the storage width, and bc is the channel width. As the water level rises from the mean low water level (MLWL) to the mean high water level (MHWL), bs increases as well as As and Ac until the intertidal area is filled with water.

Water level (m)	Section 0 (0-2 km)	Section 1 (0.5-2.5 km)	...	Section 339 (166.5-168.5 km)
10	1133	2227	...	446.5
9.9	1117	2198	...	439.9
9.8	1087	2140	...	433.5
...	...	...	...	...
-9.9	0	0	...	0
-10	0	0	...	0

Table 3.1: Table showing the average storage flow surface area (m^2)(As) calculated for each section (section length is 2 km) along the river Scheldt for water levels ranging between -10 and 10 meters relative to NAP in steps of 0.1. This table was used as input for the Scheldt bathymetric data into the 1D model.

I defined the channel of the Scheldt as the grid cells in the bathymetric data that were lower than the calculated mean low water level along the channel in 2022, taken from the data analysis. Next, I assumed that the grid cells with a depth higher than the mean low water level were part of the storage area (Figure 3.1). To implement the bathymetry of the Scheldt into the 1D model, pre-calculated tables containing various parameters (e.g., channel depth, width, area, storage depth, width, and area) for different water levels along the river were made. Each table, exemplified in Table 3.1 for the storage area, has the same standardized format.

The average values of all these parameters used in the input data tables (average channel depth, channel width, storage depth, storage width, total width, channel flow surface area, storage flow surface area, and total flow surface area) were calculated using the interpolated bathymetric data for every 500 m along the channel using a moving average. Therefore, I divided the river into 2000 m long sections, starting at 0 km at the river mouth. The sections were overlapping to create a smoother profile, and each section moved 500 m further upstream, so the first section was from 0 to 2000 m, the second from 500 to 2500 m, etc. This gave 340 sections as the river is 168.5 km long. The average value for all parameters was calculated per defined section for every water level ranging between -10 m to 10 m relative to NAP in steps of 0.1 meter.

Next, the created tables with the different bathymetric values (channel width, storage width, channel depth, storage area, etc.) for each section per water level were loaded into the model. Then, the model used linear
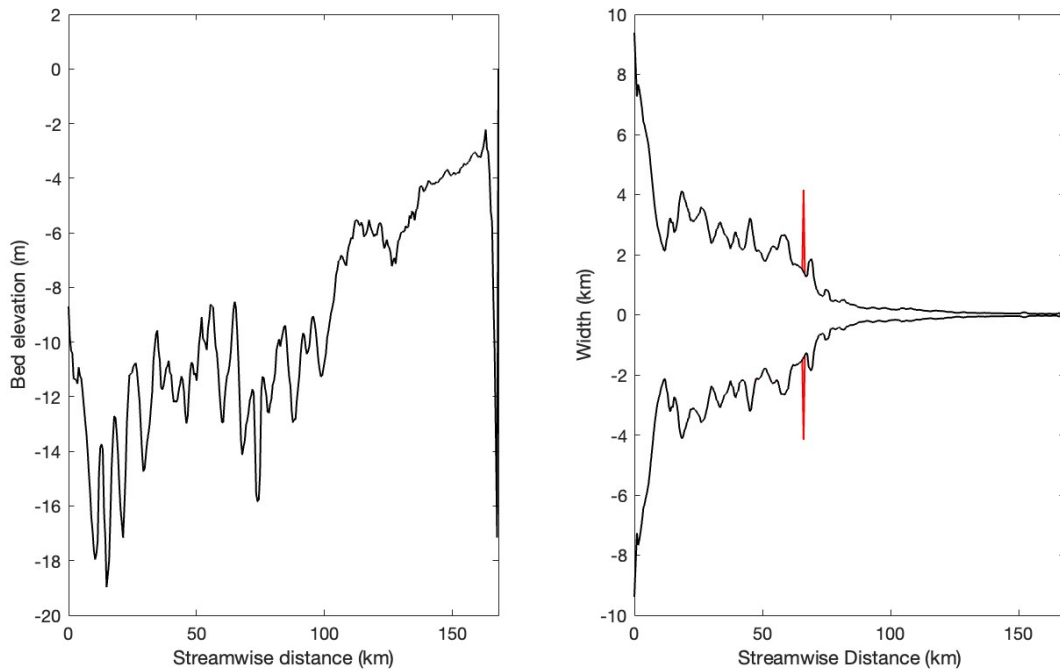
Figure 3.2: On the left, the bed elevation of the Scheldt along the channel, which was implemented in the numerical 1D model. On the right, the width of the river Scheldt from above is shown in black, which shows a converging pattern when moving further inland from left to right. The additional implemented storage area of 3000 ha is shown at 66 km in red.

interpolation to calculate the complete bathymetry of the river per water level. First, the water level was updated, after which the channel width and storage width for that water level for each point along the river were found in the input tables (values are available for every 500m). The average parameter value per section was assigned to the s-coordinate (along the channel coordinate) in the middle of the section, and for all s-coordinates in between, the values for the channel and storage width were linearly interpolated. This gave a channel and storage width for a water level of 0 m, as shown in Figure 3.2. After the water level was updated, the storage area, channel area, storage depth, and channel depth were updated similarly. The bed elevation of the Scheldt implemented like this into the model is shown in Figure 3.2. Then, for the next time step, the water level changed, and again, the tables were used to update the bathymetry of the river.

For the model runs containing an extra intertidal area, the bathymetric input tables of the parameters storage width, total width, storage flow surface area, and total flow surface area had to be adapted. For example, for one of the model runs, a polder of 3000 ha was added at 66 km, as shown in red in Figure 3.2. Therefore, the original input tables were taken for storage width, storage area, total width, and total area. At the section corresponding to the s-coordinate of 66 km, the area and width of the intertidal area were added to the already existing value for storage width and storage area once the water level became greater than the polder elevation and the total area and width were updated as well.

3.2.3 Model calibration

Other parameters that needed to be set before the model could be run beside the bathymetry of the river were the river length, the downstream boundary condition, consisting of an imposed M2, M4, and M6 tidal wave, the upstream boundary condition consisting of the discharge (m^3/s), the initial water level, and initial discharge among others. For the model calibration, I first imposed the bathymetric data together with a river discharge of 100 m^3/s and a tidal wave of $(1.90 * cos((2\pi/(12.42 * 3600)) * t - 0.5\pi))$. After that, I ran the model for 10 days during normal

tidal conditions, in which the final five tidal cycles were analyzed, and the time before was used as spin-up time. Then I performed 40 calibration runs in which the Chézy coefficient was changed for each run for values ranging between 30 and 70 $m^{0.5}/s$; I chose this range because previous research from De Gelder et al. (1996) found a suitable Chézy value of 50 $m^{0.5}/s$ to model the Western Scheldt at an average depth of 8 m. After that, I compared the tidal range, M2 and M4 amplitude, and phase calculated with the model for each run to the observed tidal range, M2 and M4 amplitude, and phase measured in the Scheldt in 2022. I used the Chézy constant from the model run that had overall the smallest root mean square error (RMSE) compared to the measured data from 2022 as the input parameter value for the investigation (All RMSE can be found in Table A.1 in the Appendix). The RMSE was calculated with the equation:

$$RMSE = \sqrt{\sum_{i=1}^{n} \frac{(\widehat{y_i} - y_i)^2}{n}} \tag{3.6}$$

Where $\widehat{y_i}$ is the predicted value along the channel, y_i is the observed value, for example, tidal range from the data analysis in 2022 along the channel, and n shows the number of observations.

After I performed all the calibration runs, the run with a Chézy coefficient of 42 $m^{0.5}/s$ showed the best performance with overall the lowest RMSE, with an RMSE for a tidal range of 0.2 m, for the M2 amplitude an RMSE of 0.11 m, and for the M4 amplitude an RMSE of 0.06. However, the RMSE for the phases of M2 and M4 was rather large for all Chézy values. After that, I used a Chézy value of 42 $m^{0.5}/s$ as an input value for the model, and I did several calibration runs to find the best upstream boundary condition, which consists of the river discharge. The upstream river discharge varied between 90 and 115 m^3/s for the different calibration runs as the average yearly discharge of the Scheldt varies between 50 and 200 m^3/s (Van Rijn et al., 2010). Optimal model performance with overall the lowest RMSE error was found for a discharge of 110 m^3/s (Table A.2 in the appendix).

Because the M4 tidal signal estimate was insufficient in previous calibration runs, I also imposed an M4 tidal wave and an M6 tidal wave at the downstream boundary beside the M2 wave already imposed in previous runs. For the implemented M4 and M6 tidal waves, the amplitude at the river mouth measured in 2022 was used. This resulted in the following downstream boundary condition:

$$H_{M_2} * cos(\omega_{M_2} * t) + H_{M_4} * cos(2 * \omega_{M_2} * t - \phi_{M_4}) + H_{M_6} * cos(3 * \omega_{M_2} * t - \phi_{M_6}) \tag{3.7}$$

H_{M_2} is the amplitude of the M2 wave, which is approximately half the tidal range measured at the mouth, with a phase of 0 degrees at the mouth. ω_{M_2} is the angular frequency of $(2\pi/(12.42 * 3600))$ because a tidal cycle in the Scheldt is around 12.5 hours which can be calculated with $\omega = 2\pi/P$ with P the period of the motion in seconds. H_{M_4} is the amplitude of the M4 wave with ϕ_{M_4} the phase difference of $2\phi_{M_2} - \phi_{M_4}$ using the average measured phases for M2 and M4 at the river mouth in 2022 to keep the ratio between M4 and M2 in line with the observed values in the field. H_{M_6} is the amplitude of the M6 wave with ϕ_{M_6} the phase difference of $3\phi_{M_2} - \phi_{M_6}$ using the average measured phases for both constituents at the river mouth in 2022, again to keep the ratio between M4 and M2 in line with the observed values in the field.

With this new downstream boundary condition, predictions for M4 and M6 improved significantly. However, the M2 tidal wave was still underestimated along the channel when looking at the M2 amplitude and tidal range. Therefore, several calibration runs were performed to find the best input value to improve the tidal range and M2 amplitude prediction. I calibrated the downstream boundary condition (Equation 3.7) for different M2 amplitudes ranging between the measured M2 amplitude at the river mouth in 2022 of 1.54 until 1.95 in steps of 0.05 m. A Chézy value of 42 and a discharge of 110 m^3/s were used, and the measured M4 and M6 amplitudes and phases at the river mouth in 2022 which were previously described. Finally, an M2 amplitude of 1.85 m showed the best results (see Table A.3 in the appendix for the RMSE of all model runs).

3.2.4 Model runs for different intertidal areas

After calibrating the model, I used the input as detailed in Table A.4 in the appendix for subsequent model runs. Various model runs were performed, using normal tidal conditions and incorporating bathymetric tables with additional

Model run	Location	Size	Elevation	Width
Run 1	No tidal flats	-	-	-
Run 2	Storage at 12 KM	3000 ha	NAP +0 m	1000 m
Run 3	Storage at 28 KM	3000 ha	NAP +0 m	1000 m
Run 4	Storage at 66 KM	3000 ha	NAP +0 m	1000 m
Run 5	Storage at 97 KM	3000 ha	NAP +0 m	1000 m
Run 6	Storage at 66 KM	3000 ha	NAP -2 m	1000 m
Run 7	Storage at 66 KM	3000 ha	NAP -1 m	1000 m
Run 8	Storage at 66 KM	3000 ha	NAP +0 m	1000 m
Run 9	Storage at 66 KM	3000 ha	NAP +1 m	1000 m
Run 10	Storage at 66 KM	3000 ha	NAP +2 m	1000 m
Run 11	Storage at 66 KM	3000 ha	NAP +0 m	1000 m
Run 12	Storage at 66 KM	3000 ha	NAP +0 m	1500 m
Run 13	Storage at 66 KM	3000 ha	NAP +0 m	2000 m

Table 3.2: An overview of the changed bathymetric variables in the different model runs. Run 1 is the control run without extra intertidal areas added. The column with location shows how many kilometers from the estuary mouth the extra intertidal area is added. The column with size shows how large the added storage area is, the column with elevation shows the height of the intertidal area, and the column with width shows the shape of the intertidal area. The width is defined as the length of the intertidal area along the channel. A larger width means that a larger part of the intertidal area is connected to the river, and the intertidal area stretches less far inland.

intertidal areas situated at different locations and featuring diverse elevations and widths. The width of the polder changed parallel to the channel. Table 3.2 provides an overview of these model runs. The output from these runs was analyzed for water level and velocity data for the final five tidal cycles of the run using T-tide in MATLAB by Pawlowicz et al. (2002). I analyzed tidal hydrodynamic changes, including tidal range, tidal prism, velocities, and amplitudes and phases of M2, M4, and M6 for each model run. Also, I focused on both vertical and horizontal tidal asymmetry to gain deeper insights into how intertidal area size, shape, and location impact tidal hydrodynamics.

Additionally, I looked into the change in tidal energy along the channel, calculated using the energy equation (Jay et al., 1990) for different scenarios:

$$\bar{e} = \frac{1}{2}\rho(g\zeta^2 + D|\vec{v}|^2) \tag{3.8}$$

With e the total energy per unit area, ρ the density of water, g the gravitational constant (m/s^2), ζ the tidal elevation (m), $D = d + \zeta$, where D is the water level, and d is the water depth between the bed and MLWL. $\vec{v}$ is the velocity vector along the channel (m/s). I also looked into the changes in tidal energy flux averaged over a single tidal cycle along the channel using equation 3.9 to investigate if the reflection of the tidal wave would occur after wetland restoration.

$$\vec{E_f} = \frac{1}{T}\int_0^T \rho D\left(g\zeta + \frac{1}{2}|\vec{v}|^2\right)dt \tag{3.9}$$

Furthermore, I investigated changes in the various terms of the continuity and momentum equations (Equations 3.4 and 3.5) to gain insights into the underlying processes driving the changes in tidal hydrodynamics to find an answer to the third sub-research question. Most importantly, I focussed on the change in the frictional term over time and along the channel after implementing an intertidal area.

Unfortunately, after performing the model runs, a numerical artifact was found in the results, suggesting a hydraulic jump or a mistake in the numerical scheme that was used.

$$C = \frac{\sqrt{gh} \cdot \Delta t}{\Delta x} \tag{3.10}$$

Reducing the time step from five seconds to half a second did not help solve the issue, which kept presenting even though the Courant number calculated with Equation 3.10 (Courant et al., 1967) for a maximum wave height (h) of 3.5 meters and a time step (Δt) of five seconds and Δx of 100 m was smaller than one (only 0.3) and would therefore suggest numerical stability, but it is not guaranteed. To better interpret the results in the results section, a moving average over five kilometers was taken for the MHWL, MLWL, and tidal range to remove the numerical artifact from the graphs.

4 | Results

4.1 Data analysis

4.1.1 Tidal hydrodynamics of the Scheldt

For this part of the results section, a reference is made to the names of several measurement stations along the Scheldt; Figure 2.1 in the field description shows a map of the area with all stations used and their names. To answer the first and second sub-research questions about the changes that occur after the opening of the Hedwige-Prosperpolder, the tidal hydrodynamics under normal conditions in the Scheldt should be understood first. The Scheldt has a semidiurnal tide. After performing a harmonic tidal analysis for each station along the river for the time period of a year before the opening of the Hedwige-Prosperpolder, a total of 59 tidal constituents were found, with over 26 significant constituents, including M2, M4, M6, and several overtides. The upstream discharge was, on average, 120 m^3/s in 2022 and visibly influences the tidal signal, especially in the Belgium part of the estuary, and becomes less the more you move toward the mouth of the river.

When analyzing the average tidal range for the year 2022, it showed that for the Scheldt estuary, the tidal range increases from 3.3 m at the river mouth to 5.3 m at 115 km further landward, just behind Antwerp. This increase in tidal range is mainly caused by the decreasing depth and the funneling bathymetric characteristics of the estuary. After Antwerp, the tidal range decreases to 2.7 m near Gent (Figure 4.1).
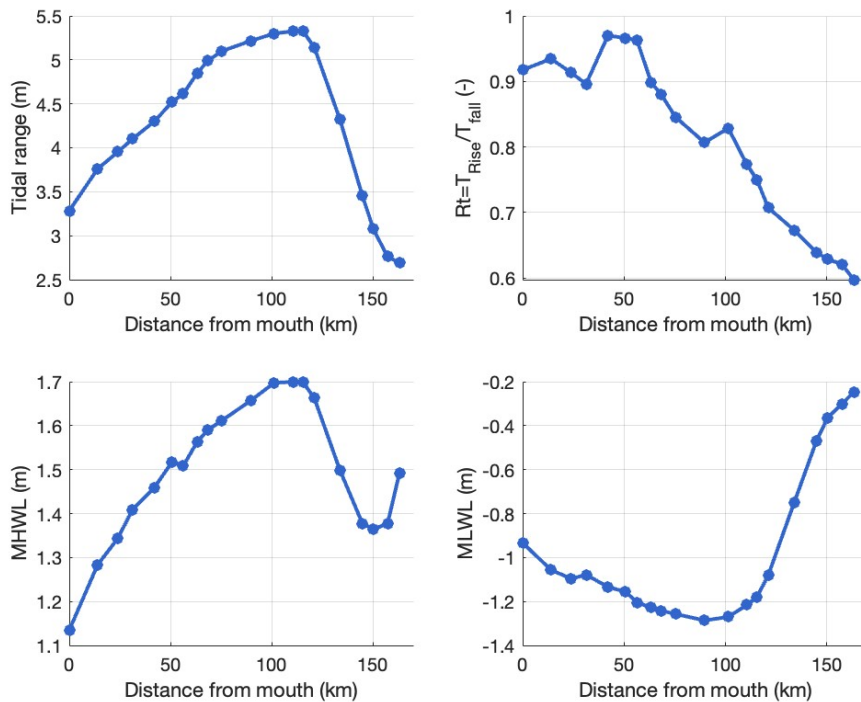
Figure 4.1: The tidal range along the channel for the year 2022 in meters. Rt equals the time of rising tide divided by the time of falling tide and indicates tidal asymmetry along the channel. Furthermore, the mean high water level (MHWL) along the channel and the mean low water level (MLWL) along the channel in meters are also shown.

The mean high water level (MHWL) shows a similar pattern as the mean tidal range along the channel, with an increase in MHWL from the river mouth towards Antwerp due to the funneling of the estuary, after which it decreases again due to a decreased channel depth. For the mean low water level (MLWL), a mirrored pattern was shown in

the same range as the MHWL. First, the MLWL decreases towards Antwerp, increasing again towards Gent, which is the highest. At Gent (168 km), the average MLWL and the MHWL increase again due to the river discharge (Figure 4.1).

Additionally, the tidal asymmetry of the system can be considered by $R_t = T_{Rise}/T_{Fall}$, which describes the ratio between the average time it takes for the tide to rise divided by the average time it takes for the tide to fall. In case R_t equals one, there is no tidal asymmetry, and the time it takes for the tide to rise is equal to the time it takes to fall. When R_t is greater than one, it indicates a larger rising time than falling time, meaning the system is ebb dominant. When R_t is between one and zero, it indicates larger falling than rising tides, meaning a flood-dominant system exists. For the Scheldt, R_t is along the entire channel smaller than one, which indicates a flood-dominant system. The amount of flood dominance overall increases when moving from the river mouth towards Gent (Figure 4.1).
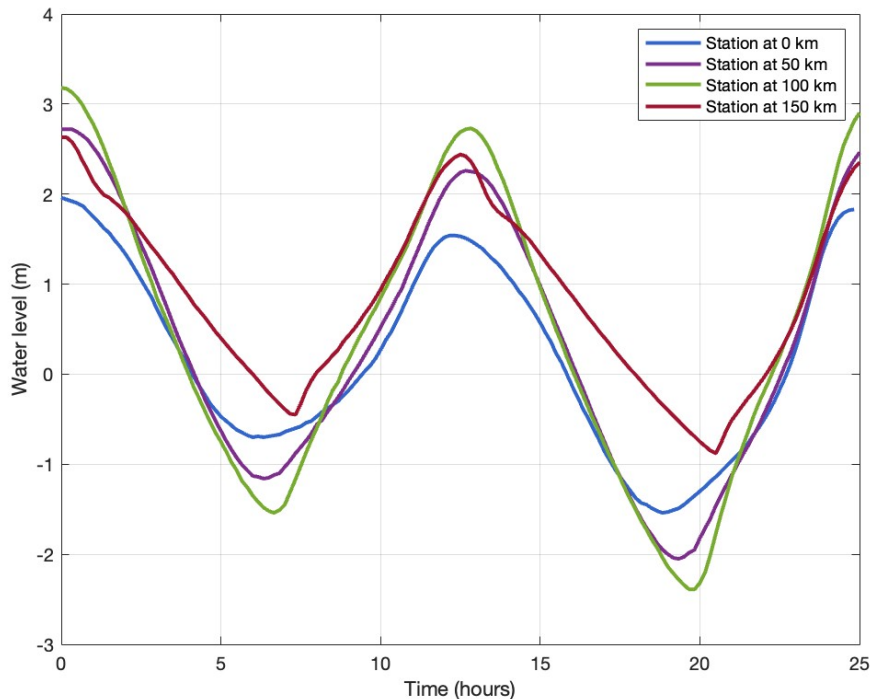

Figure 4.2: The tidal curve at four locations from the mouth over two tidal cycles (25 hours) for October 6th, 2022. Measurement station Westkapelle is located at the mouth of the river Scheldt (0 km), Walsoorden is located 50 km from the mouth, Hemiksem is 100 km, and Uitbergen is around 150 km from the river mouth.

When considering the tidal asymmetry in the Scheldt using the water level data gathered in 2022, the observed representative tidal wave during normal tidal conditions in 2022 at the river mouth shows a falling time of first 6 hours and later 6.5 hours and a rising time of first 6 hours and later 6 hours and 20 minutes. Overall, the time difference between falling and rising time for the station Westkapelle is similar. However, when moving further landward, the rising time of the tidal wave slowly decreases, and the falling time increases over time. As a result, the tidal wave deforms and becomes more asymmetric as it moves landward. For the station at 50 km from the mouth, not much change is visible in rising and falling time yet. The average falling time becomes 6.5 hours and is 15 minutes greater than at the river mouth. Here, the average rising time is 6 hours and 10 minutes, equal to the rising time at the river mouth (Figure 4.2).

For the station, Hemiksem at 100 km from the mouth, tidal asymmetry increases as the average falling time is 6 hours and 50 minutes (35 minutes more than at the mouth), and the average rising time decreases towards 5 hours, which is 70 minutes less than at the mouth. For the station at 150 km, the average falling time is 7 hours and 40 minutes, almost an hour longer than at the mouth. The average rising tide here is 5 hours, 70 minutes less

than at the mouth (Figure 4.2). This shows that the tidal asymmetry increases when moving further landward, as the time difference between falling in rising time becomes more pronounced, and the overall shorter rising tide than falling tide points towards an increase in flood-dominant tidal asymmetry, which is also observed in the calculated R_t value in Figure 4.1.
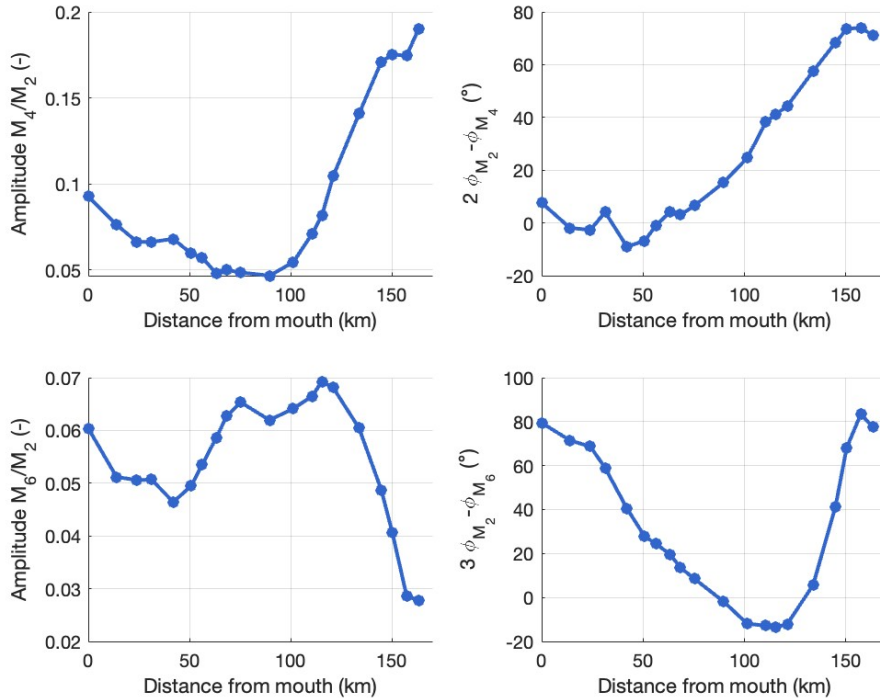

Figure 4.3: The amplitude ratio of the M_4/M_2 tidal wave and the amplitude of the M_6/M_2 tidal wave indicate the amount of tidal asymmetry. Also, the $2\phi_{M_2} - \phi_{M_4}$ and $3\phi_{M_2} - \phi_{M_6}$ phase differences along the channel are shown.

When considering a tidal constituent analysis of M_2, M_4, and M_6 in the Scheldt, overall, the magnitude of the M_4 constituent is greater than that of the M_6 constituent. The M_4/M_2 amplitude ratio indicates the strength of vertical asymmetry, which decreases from Vlissingen to Antwerp for the Scheldt and increases when moving landward from Antwerp. The influence of M4 on M2 displays asymmetry, impacting one segment of the tidal cycle differently from the other. Furthermore, the $2\phi_{M_2} - \phi_{M_4}$ phase difference serves as an indicator for the nature of the vertical asymmetry of the river and is considered representative of phase differences between other quarter diurnal and semi-diurnal constituents. A phase difference between 0 and 180 degrees is considered flood dominant, indicating faster water movement during floods and more sediment transport into the estuary. Conversely, ebb dominance is assumed for a phase difference between -180 and 0 degrees, meaning water flows faster during ebb tide.

In the case of the Scheldt, the phase difference between M2 and M4 is around zero or slightly below until 50 km from the river mouth, after which it increases towards 80°, indicating that the tidal asymmetry increases when moving further inland. Pronounced variation in width occurs around 50 km, which could explain this increase in tidal asymmetry. Because of the decreasing depth and width of the estuary, friction increases, and low-water propagation slows more than high-water propagation, resulting in increased flood dominance.

The generation of the M6 overtide is mostly due to frictional effects. The impact of M6 on M2 exhibits symmetry, meaning it affects both high tides and low tides uniformly. Also, M6 can affect the overall tidal range. For the Scheldt river, first, an increase in the M_6/M_2 amplitude ratio is shown until Antwerp. It is expected this is caused by increased friction along the channel, generating the M6 overtide. After 120 km, a decrease in the M_6/M_2 amplitude ratio is shown for the remaining part of the river. As for the phase difference of $3\phi_{M_2} - \phi_{M_6}$, the phase difference decreases from 80 degrees until -10 degrees near Antwerp after which it increases again to 80 degrees near Gent (Figure 4.3).

This shows that the sixth diurnal tide plays an important role in the Scheldt, and it suggests along-channel changes in the asymmetry of the tidal wave due to the M6 overtide.

4.1.2   Change in tidal hydrodynamics in the Scheldt after the opening of the Hedwige-Prosperpolder

In October 2022, the Hedwige-Prosperpolder was opened, giving the Scheldt more space to flow during high tide. Therefore, in this chapter, changes in tidal hydrodynamics between 2022 and after the opening in 2023 were investigated to be able to answer the first and second sub-research questions. For the tidal range, an overall decrease along the channel was shown (Figure 4.4). The tidal range decreases with 2 cm at the mouth and 6 cm just past the Hedwige-Prosperpolder at the station called Liefkenshoek (abbreviation: LIEF), after which the decrease in tidal range becomes less. However, the seventh station, Overloop van Hansweert (abbreviation: OVH at 52 km), just before the intertidal area, shows a slight increase in the tidal range due to a slight decrease in mean low water level, which deviates from the patterns visible for the other stations. When considering the difference in tidal range per station between other years in which no significant bathymetric changes have occurred, a difference of 2 cm at the mouth and 6 cm around Antwerp is not unusual and, therefore, can not be attributed to the opening of the intertidal area alone (Table B.1 in the appendix).
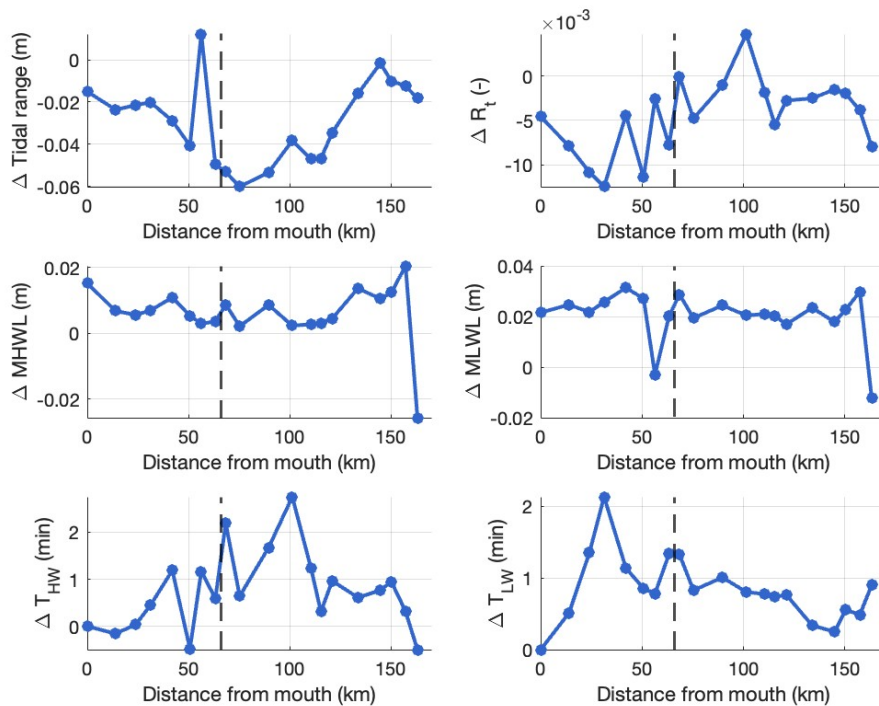
Figure 4.4: Change in the tidal range between the year after the opening of the Hedwige-Prosperpolder (2023) and the year before the opening of the intertidal area (2022) is visible along the channel. $R_t = T_{Rise}/T_{Fall}$, which describes the ratio between the average time it takes for the tide to rise divided by the average time it takes for the tide to fall and is a measure of tidal asymmetry. Here, the difference in R_t is shown between 2023 and 2022. Furthermore, the mean high water level (MHWL) changes between 2023 and 2022. The change in mean low water level (MLWL) between the year after the opening of the intertidal area and the year before is visible. The phase differences between high water (T_{HW}) and low water (T_{LW}), respectively. In all sub-figures, the dotted line represents the location of the Hedwige-Prosperpolder along the Scheldt at 66 km from the mouth.

Furthermore, the mean high water level (MHWL) increases a little along the channel with a maximum of 2 cm. Still, no significant changes occurred for this parameter around the intertidal area (Figure 4.4). Moreover, the variation in MHWL between other consecutive years along the channel can be much greater than the observed

changes between 2022 and 2023 (Table B.2 in the appendix). For the mean low water level (MLWL), an average increase of approximately 2 cm is visible along the channel (Figure 4.4). The station called Overloop van Hansweert shows an outlier of a slight decrease in MLWL again. This is, however, not unusual for this station and can occur at other stations for other years as well. Still, overall, the changes in MHWL and MLWL are a lot smaller than the maximum changes between other consecutive years (Table B.3 in the appendix) and are, therefore, not significant enough to be able to conclude that these occurred because of the increase in intertidal area and not due to dredging, a change in river discharge, or changes in tidal forcing from the North Sea.

The phase difference between high water (T_{HW}) and low water (T_{LW}), which serves as an indicator for tidal asymmetry, generally increases for the year 2023, when the intertidal area is opened. Still, no significant changes are shown around 66 km where the intertidal area is located compared to the remaining part of the channel (Figure 4.4). The maximum increase in high water travel time is at the location of the Hedwige-Prosperpolder 2 minutes. This is not an unusually high water phase difference between consecutive years (Table B.4 in the appendix). For the travel time of low water, a maximum increase of 1.5 minutes is visible at the location of the intertidal area, which is also not an uncommon change for this location between consecutive years (Table B.5 in the appendix). Furthermore, even though the intertidal area is opened, the estuary stays flood-dominant, with little change in R_t ($R_t = T_{rise}/T_{fall}$) between the two consecutive years.

Besides water level data, point velocity measurements were also analyzed and showed an average maximum flood velocity of 0.874 m/s and an average maximum ebb velocity of -0.992 in 2022. The higher ebb velocities indicate ebb dominance for the horizontal tidal asymmetry of the system. For the year after the opening of the intertidal area, an average maximum flood velocity of 0.935 m/s and an average maximum ebb velocity of -1.046 were found. This shows a slight increase in both parameters of 7% for the flood velocity and 5.5 % for the ebb velocity. However, when analyzing the point velocity data for the same point from 2010 until 2015, percentile differences between consecutive years vary from less than 1 % to 63 %. This makes it impossible to conclude that the change in intertidal area due to the opening of the Hedwige-Prosperpolder resulted in changes in the average maximum flood and ebb velocity (Table B.6).

Additionally, velocity measurements were used in harmonic tidal analysis to investigate changes in amplitude and phase of M_2, M_4, and M_6. These showed a slight increase in amplitude for 2023 compared to 2022 for all three constituents, which is larger than the error margin for M_2 and M_4. The phase of the constituents decreased in 2023 compared to 2022 for all three, but the decrease was smaller than the error margin for all three. These results suggest that no large changes in the phase and amplitude of the constituents considered were caused by the opening of the Hedwige-Prosperpolder (Table 4.1).

	2022	**2023**	Δ
M_2 **Amplitude (m/s)**	0.0878 ± 0.016	0.935 ± 0.014	0.057 ± 0.030
M_2 **Phase (∘)**	66.9 ± 0.96	65.7 ± 0.91	-1.2 ± 1.8
M_4 **Amplitude (m/s)**	0.0319 ± 0.0071	0.0338 ± 0.0087	0.0019 ± 0.016
M_4 **Phase (∘)**	192 ± 14	189 ± 23	-3.11 ± 37
M_6 **Amplitude (m/s)**	0.107 ± 0.014	0.112 ± 0.014	0.005 ± 0.027
M_6 **Phase (∘)**	7.49 ± 7.3	5.52 ± 7.3	-1.97 ± 15

Table 4.1: An overview of the calculated M_2, M_4, and M_6 amplitude and phases as a result of the tidal harmonic analysis using velocity data, measured the year before and after the opening of the intertidal area with their error margins.

4.2   Model study

4.2.1   Effect of different locations of intertidal area implementation

To answer the third sub-research question, the effect of the location of intertidal areas on the changes in tidal hydrodynamics and the most important mechanistic processes involved were investigated. Four model runs were performed with an intertidal area of 3000 ha. The wetlands were implemented for different runs on 12, 28, 66, and 97 km. The change in tidal range compared to before the implementation shows, for all situations, a decrease in tidal range along the channel, which is greater if the intertidal area is located further landward. The decrease in tidal range is greatest just before the intertidal area and can be up to 6 cm for an intertidal area located at 97 km (Figure 4.5). The MHWL shows the same pattern as the tidal range, and the MLWL shows a slight increase along the channel after the intertidal area increases. This increase in MLWL becomes larger and can be up to an increase of 4 cm around 150 km from the mouth for an intertidal area at 97 km (Figure 4.5).
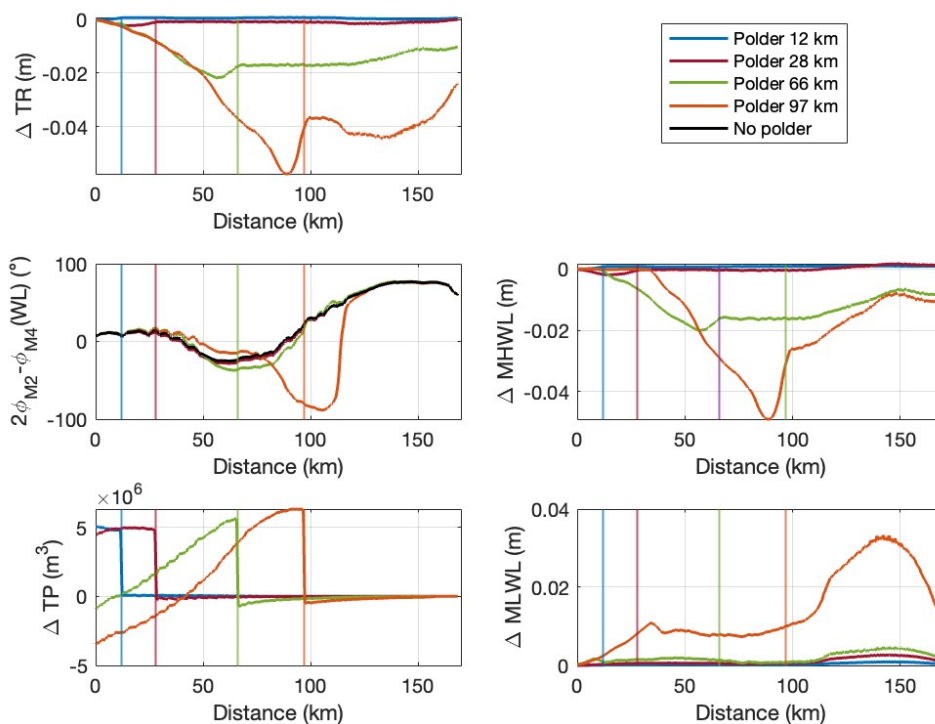

Figure 4.5: An overview of the change in tidal range (TR) along the channel for the four scenarios. Underneath, the phase difference between the M_2 and M_4 tidal constituents per model run are shown along the channel, calculated using water level data (WL). Underneath, a graph of the tidal prism (TP) is visible. On the right, the change in mean high water level (MHWL) along the channel and mean low water level (MLWL) between the run without extra tidal area and with is shown. The vertical lines show the locations of the intertidal areas.

The phase difference between M_2 and M_4 of the vertical tide, using water level data, for the Scheldt without adding extra intertidal areas shows a flood-dominant asymmetry between 0 and 28 km and between 80 and 170 km. In between, the system experiences some ebb-dominant asymmetry. When adding an intertidal area at 12 or 28 km, no visible change in asymmetry occurs. However, the phase difference between M_2 and M_4 of the vertical tide shows increased ebb dominance at the location of the intertidal area at 97 km (orange line) compared to the model run without extra intertidal area (black line), as a negative phase difference is considered as ebb-dominant asymmetry. The same effect is visible for the intertidal area at 66 km around the location of the intertidal area but is less pronounced (Figure 4.5).

For the flood tidal prism, the implementation of the intertidal area at 12 and 28 km shows an increase in flood tidal prism from the river mouth until the intertidal area, indicating that because of enough available water in the North Sea, more water is transported into the river during a flood to fill the intertidal area. For implementing an intertidal area at 66 and 97 km, an increase in tidal prism seaward of the intertidal area is visible due to the increased storage capacity during the flood, as more water can flow into the intertidal area. Interestingly, the tidal prism decreases at the river mouth for the intertidal areas at 66 and 97 km. Additionally, a small decrease in tidal prism is visible landward of the intertidal area because more water is stored in the intertidal area and no longer travels landward (Figure 4.5).
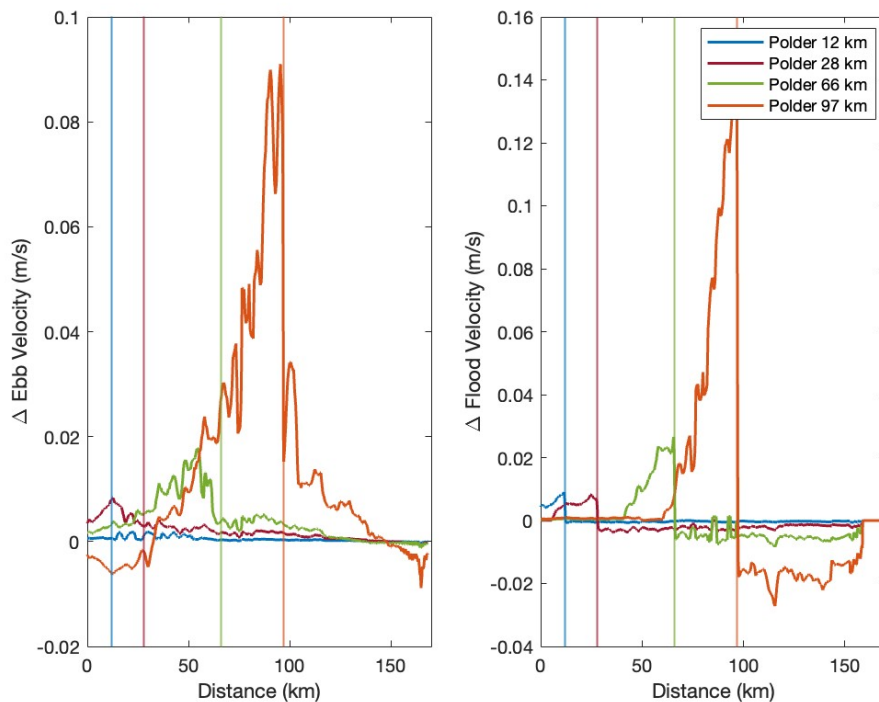

Figure 4.6: Change in average ebb and flood velocity along the channel. The vertical lines show the locations of the intertidal areas implemented in the different model runs.

Following the expansion of the intertidal area, the average ebb velocity in the channel significantly increases along the channel, and again, this effect is greater for an intertidal area located more landward. The effect is not visible for the intertidal area near the river mouth at 12 km. For intertidal areas at 66 and 97 km, the greatest increase in ebb velocity is visible just seaward of the implemented intertidal area. Even a slight decrease in ebb velocity is visible at the river mouth for the intertidal area implemented at 97 km. The effect of implementing extra intertidal area is greater on the flood velocity than the ebb velocity. An increase is visible for the average flood velocity just before the opened intertidal area, which becomes larger for a more landward-located intertidal area. The increase in flood velocity is almost twice as large as the increase in ebb velocity. Landward of the implemented intertidal area, the flood velocity decreases compared to the situation without extra intertidal areas (Figure 4.6).

Also, the friction in the channel was analyzed using the frictional term from the momentum equation described in equation 3.5. This showed that a change in increased flood velocity before the intertidal area and a decrease after leads to a significant increase in friction in the channel before the intertidal area and a small decrease in friction due to a decreased velocity further landward of the intertidal area. Furthermore, the friction also decreased at the river mouth due to decreased ebb velocity (Figure 4.6 and C.1 in the appendix).

When an intertidal area is opened adjacent to the channel, and the water level in the channel rises during high tide, a sharp water gradient develops in the channel towards the intertidal area as soon as the water level is sufficiently

high to allow flow into the intertidal area. Because of this steep water level gradient, the flow velocity in the channel increases (Figure 4.6), and the intertidal area will fill up with water quickly. Then, the channel's water level also decreases right before the polder. Also, because of the increased flow velocity in the channel, the channel's friction increases, resulting in the decrease in tidal range along the channel shown in Figure 4.5.

For the energy balance, consisting of kinetic and potential energy averaged over a tidal cycle, there is a change in total energy along the channel when creating an extra intertidal area. Little change in potential energy occurs for the intertidal area near the mouth. For the intertidal area at 28 km, there is a slight decrease in potential energy before the intertidal area. This decrease is larger for the other two intertidal areas further inland, with a maximum decrease just before the intertidal area. The decrease in potential energy is also spread over a longer distance along the channel. However, the kinetic energy increases before the intertidal area, and this effect becomes more severe when creating an intertidal area further inland. This increase in kinetic energy correlates with the visible increase in ebb and flood velocity before the intertidal area. The total energy shows a combination of the two. For the intertidal area at 97 km from the mouth, the increase in kinetic energy is almost twice as large as the decrease in potential energy. Therefore, the total energy increases at the location of the intertidal area and seaward of the polder. Still, it goes down further away from the intertidal area as there is very little change in kinetic energy here, but the potential energy still goes down because of a decrease in MHWL (Figure 4.7).

For implementing the polder at 97 km, the largest decrease in tidal range coincides with the greatest increase in total tidal energy. When analyzing the energy flux along the channel for one tidal cycle, an increase is visible before the polder, which shows a similar pattern as the kinetic energy, suggesting there is almost no reflection of the tidal wave visible as, in that case, a decrease in energy flux seaward of the polder was expected (Figure 4.7).
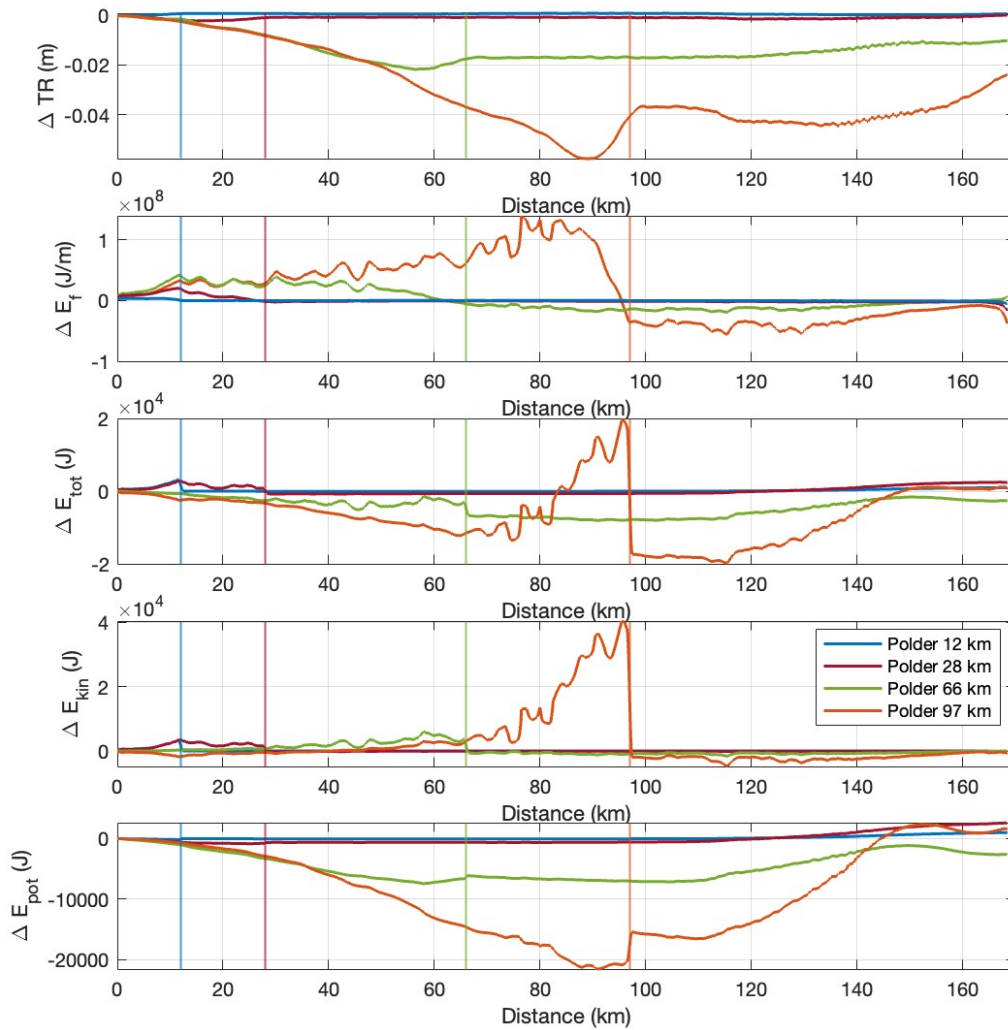
Figure 4.7: Change in tidal range (TR), change in tidal energy flux averaged over a single tidal cycle over the cross-section (E_f), total (E_{tot}), kinetic (E_{kin}), and potential (E_{pot}) tidal energy along the channel averaged over a single tidal cycle. The vertical lines show the locations of the intertidal areas implemented in the different model runs.

4.2.2   Effect of different elevations for intertidal area implementation

To answer the third sub-research question, the effect of the elevation of intertidal areas on the changes in tidal hydrodynamics and the most important mechanistic processes involved were investigated. Therefore, five model runs were performed with intertidal areas implemented at 66 km from the river mouth with a total area of 3000 ha. In each model run, the intertidal area had a different elevation, ranging between -2 m and +2 m in height from NAP. When considering the tidal range, just like for previous model runs, the tidal range decreases along the channel after implementing an intertidal area, and the decrease is greatest just seaward of the intertidal area. When looking at the effect of different elevations, the decrease is greater for an intertidal area at -2 m compared to 2 m as the storage capacity is larger and more water can flow into the area for longer. This change in tidal range is mainly caused by the decrease in MHWL, which decreases more for a lower intertidal area due to more storage capacity in the intertidal area. The MLWL shows an overall increase in water level after intertidal area implementation, which is greater when the intertidal area is on a lower elevation. No significant change is visible for the intertidal areas above 0 NAP (Figure
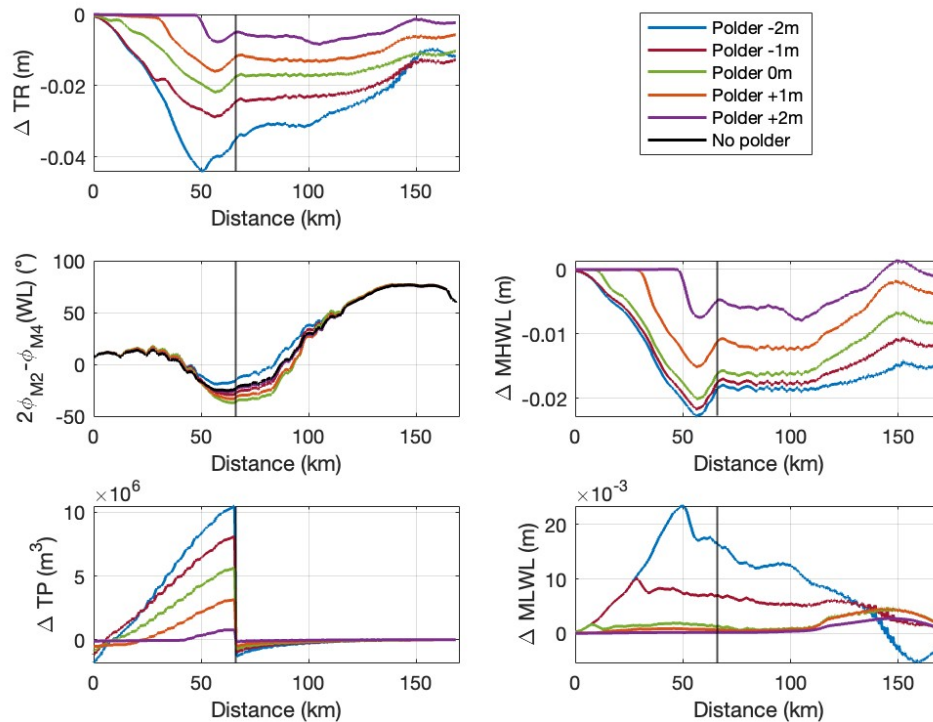
4.8).

Figure 4.8: An overview of the change in tidal range (TR) along the channel for the five scenarios with different elevations of an intertidal area of 3000 ha at 66 km. Underneath, the phase difference between the M_2 and M_4 tidal constituents per model run are shown along the channel, calculated using water level data (WL). A graph of the change in flood tidal prism (TP) is shown below. On the right, the change in mean high water level (MHWL) along the channel and mean low water level (MLWL) between the run without extra tidal area and width is shown. The vertical line shows the location of the intertidal area.

The phase difference between M_2 and M_4 calculated with water level data shows a decrease in ebb-dominant vertical asymmetry for an intertidal area of -2 m around 66 km. There could be a decrease in ebb-dominance for an intertidal area at this elevation due to decreased friction (Figure C.2 in the appendix) due to a deeper water level than the intertidal areas at higher elevations. For the intertidal area of -1, +1, and +2 m, there is a small increase in ebb-dominant vertical asymmetry around the intertidal area, possibly because of lower water depths in the tidal area, resulting in increased friction and a decrease of the water velocity during high tide. For an intertidal area at 0 m, the increase in ebb-dominant vertical asymmetry is the largest (Figure 4.8).

The flood tidal prism increases before the intertidal area for all elevations. This increase in tidal prism in the intertidal area is greatest for an elevation of -2 m as that intertidal area has the highest storage capacity, and it is lowest for the intertidal area of +2 m but still visible. Landward of the intertidal area, a small decrease in tidal prism is visible, which is greatest for the intertidal area of -2 m. Again, a decrease in the tidal prism is visible at the river mouth, but only for the intertidal areas at +1m, 0m, and -1 m, and a slightly larger decrease for the intertidal area at -2 m (Figure 4.8).

The effect of elevation of extra intertidal areas on the ebb velocity shows the largest increase in velocity before the intertidal area for elevations of -2 and -1 m, less for 0 m and +1 m and almost none for an intertidal area of +2 m. Almost no increase in velocity for an elevation of +2 m is visible because, generally, the mean water level in the estuary for this model is not above two meters, so for this scenario, the intertidal area is not flooded often. Landward of the intertidal area, the ebb velocity also increased but was less than seaward of the area for elevations of +1 m, 0 m, and -1 m. An intertidal area of -2 m even shows a significant decrease in ebb velocity landward of

the intertidal area. For the change in flood velocity after intertidal area implementation, the flood velocity increases before the intertidal area for all elevations, but most significantly for -2 m elevation. After passing the intertidal area, the flood velocity in the channel decreases only for the intertidal areas with an elevation of 1m, 0m, and -1m and not significantly for the intertidal area at -2 and +2 m (Figure 4.9). The friction along the channel has a linear relationship with the velocity, showing the same pattern (Figure C.2 in the appendix). Because the average ebb and flood velocity increase before the intertidal area for all elevations except +2 m, the friction also increases along this section due to the increased velocity for those situations.
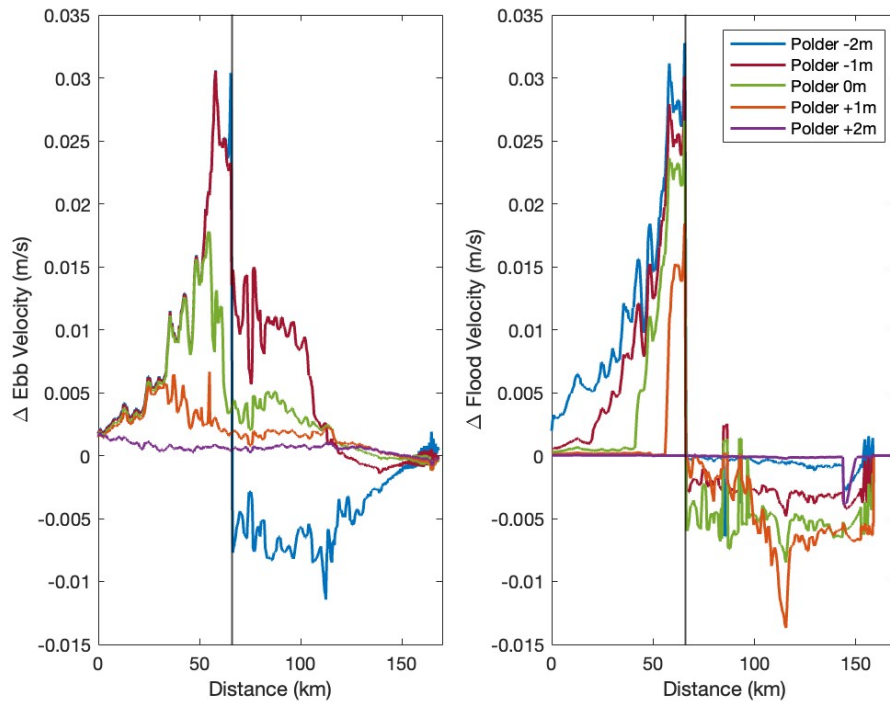

Figure 4.9: Change in the ebb and flood velocity for an intertidal area of 3000 ha at 66 km on different elevations. The vertical black line shows the location of the intertidal area.

When considering the change in total tidal energy averaged over a single tidal cycle along the channel, almost no change is visible for an intertidal area at 2m height. However, as shown in figure 4.10, the lower the tidal area is implemented, the larger the decrease in total energy, which is the largest just after the implemented intertidal area. For the kinetic tidal energy, an increase is visible before the intertidal area, which is larger the lower the intertidal area is implemented. After the intertidal area, the kinetic energy decreases a bit in accordance with the change in velocity along the channel. A decrease along the channel after implementing the extra intertidal area is visible for the potential energy. The decrease is much larger than the increase in kinetic energy. Therefore, the total energy decreases along the entire channel after tidal area implementation (Figure 4.10). This result is also in accordance with the decrease in MHWL visible in Figure 4.8.

The difference in the tidal range also shows that the largest decrease corresponds with the smallest decrease in total tidal energy along the channel. Another interesting observation is the increase in total energy, potential energy, and tidal range further inland, which a backwater effect could cause due to flow constriction upstream of the river. For the tidal energy flux over a single tidal cycle, an increase is visible around 5 km before the location of the added intertidal area, which is greater for a polder at a lower elevation. No increased reflection of the tidal wave can be observed when lowering the elevation of the intertidal area (Figure 4.10).

Certain patterns are visible when considering the change in several parameters at the intertidal area site over time. Examining the change in storage area over time for a model run without intertidal area at 66 km and for one
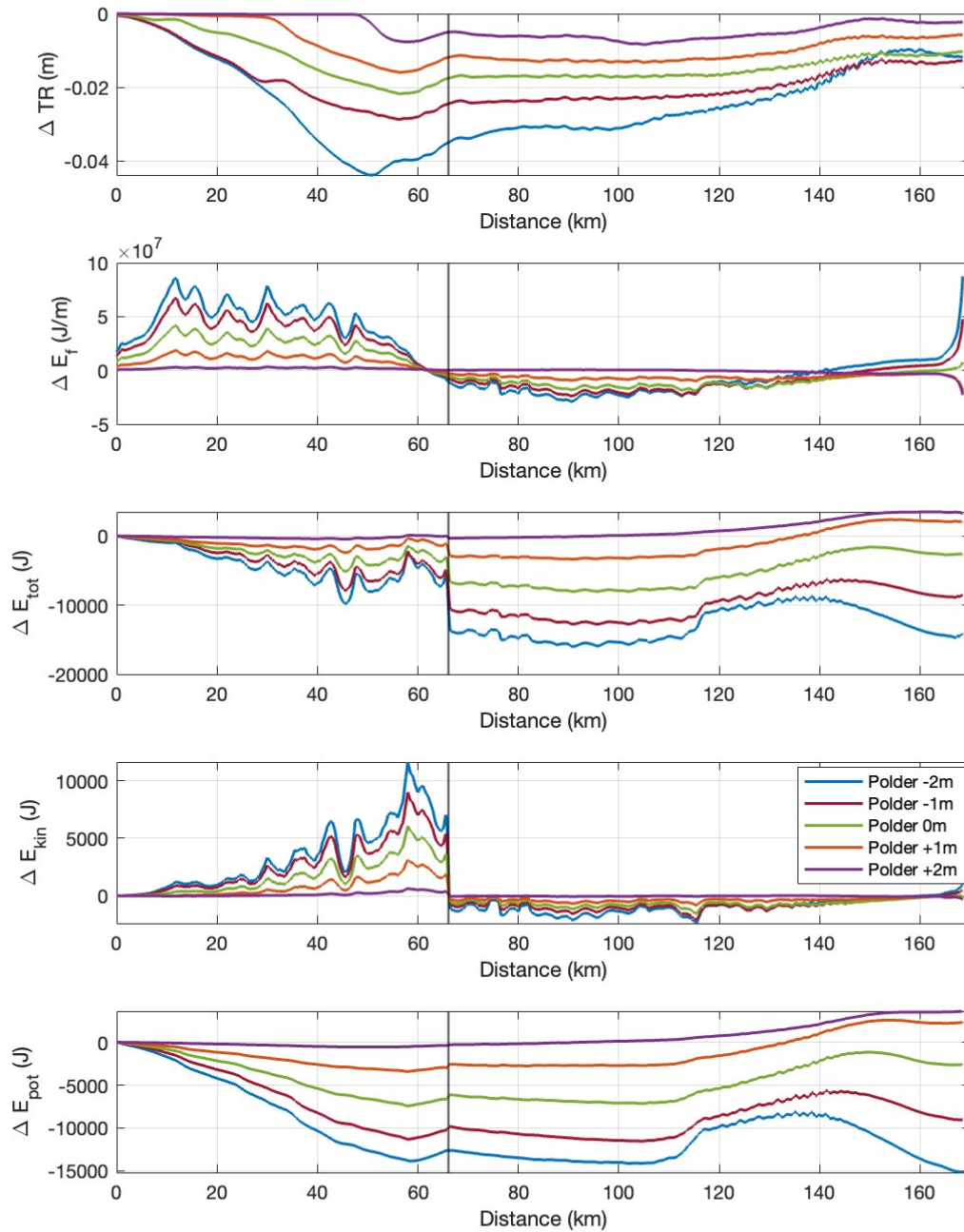
Figure 4.10: Change in tidal range (TR), change in tidal energy flux averaged over a single tidal cycle over the cross-section (E_f), total (E_{tot}), kinetic (E_{kin}), and potential (E_{pot}) tidal energy along the channel averaged over a single tidal cycle. The vertical line shows the location of the intertidal areas implemented in the different model runs.

with intertidal area implemented at +1m elevation over a tidal cycle. Comparing figure 4.11 and 4.12 shows that the storage area significantly increases when an intertidal area is added to the system and that at first, the intertidal area slowly increases with the water level and as soon as it can enter the polder the storage area increases drastically.

Figure 4.11: The change in water level (h) and velocity (u). The change in total energy, potential energy, kinetic energy, and friction. The bottom graph of the channel and storage area has a logarithmic y-axis and shows the time over one tidal cycle (12.5 hours) for a model run without any additional intertidal area.

The pattern of friction over time, which increases with velocity, is not influenced by adding the storage area in the model. It already starts increasing before the intertidal area is used for water storage when the velocity in the channel increases and reaches its maximum of around 8 hours for both scenarios. Furthermore, potential energy is greatest at high and low water levels and lowest for the transition between high and low tide. For the kinetic energy, it is the other way around, as velocity is lowest during high and low water and greatest in between. Also, the energy at the specific location of the polder does not seem to change much over time after adding the storage area. When considering the velocity and water level change over time for both situations, high and low tide coincides with slack water, showing velocity and water level are out of phase, indicating a standing tidal wave. This does not change when an intertidal is added to the system.
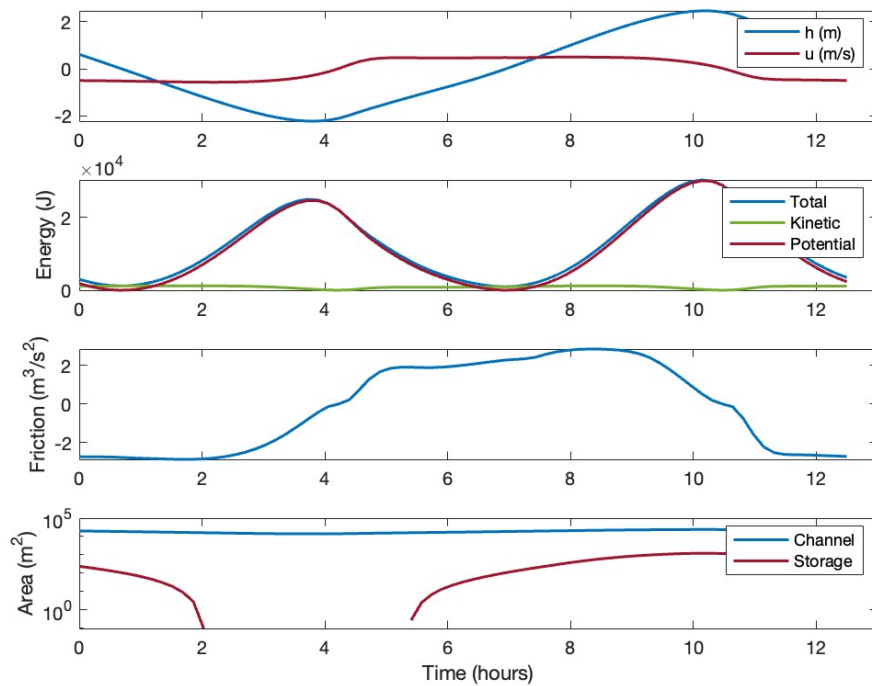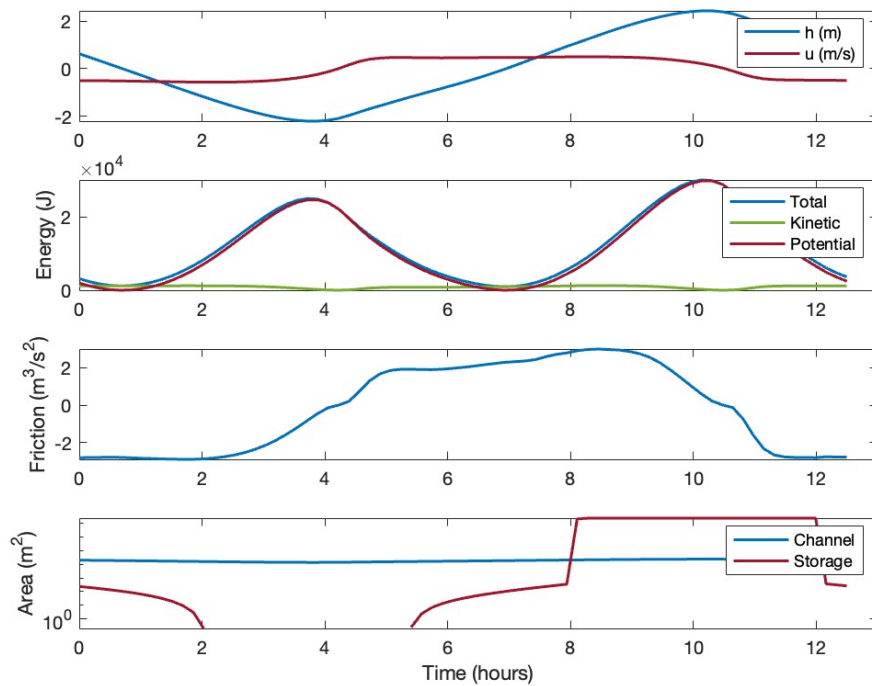
Figure 4.12: The change in water level (h) and velocity (u). The change in total energy, potential energy, kinetic energy, and friction. The bottom graph of the channel and storage area has a logarithmic y-axis and shows the time over one tidal cycle (12.5 hours) for a model run with an additional intertidal area of 3000 ha at +1 m elevation.

4.2.3 Effect of different different shapes for intertidal areas

To answer the third sub-research question, the effect of the shape of intertidal areas on the changes in tidal hydrodynamics and the most important mechanistic processes involved were investigated. Therefore, three model runs were performed with intertidal areas implemented at 66 km from the river mouth with a total area of 3000 ha but with three different along channel widths: 1 km wide, 1.5 km wide, and 2 km wide. The tidal range shows a more significant decrease for a wider intertidal area of 2 km compared to a less wide intertidal area of 1 km. The Tidal range decreases up to 4 cm before the intertidal area of 2 km wide; landward of the intertidal area, a stable decrease of around 3 cm is visible. The same applies to the other two scenarios, but the effect is overall less. The same pattern is visible for the MHWL, with the steepest decrease just before the intertidal area for the intertidal area with a 2 km width. Because of the increased width, a larger part of the channel is influenced by the increased storage area, reducing the MHWL more for a wider intertidal area. The MLWL shows a small increase along the channel, which becomes larger further landward but is still at the maximum, only an increase of 1.5 cm (Figure 4.13).

The phase difference between M_2 and M_4 calculated with water level data shows increased ebb-dominance in the vertical asymmetry around the intertidal area for all three shapes, but the most for the widest intertidal area. The remaining part of the river shows flood dominance for the vertical tide (Figure 4.13). Flood dominance occurs near the river mouth and further landward and is not influenced by the addition of intertidal area. For the flood tidal prism, there was an increased tidal prism just before the implemented intertidal area at 66 km for all widths, with a slight decrease afterward. The increased tidal prism landward slowly decreases towards the river mouth. At the river mouth, a decrease of flood tidal prism is visible. The flood tidal prism increases the most for the widest polder of 2 km at 66 km and decreases the most at the mouth, but here, the difference for the intertidal areas of different widths is less pronounced than further landward (Figure 4.13).
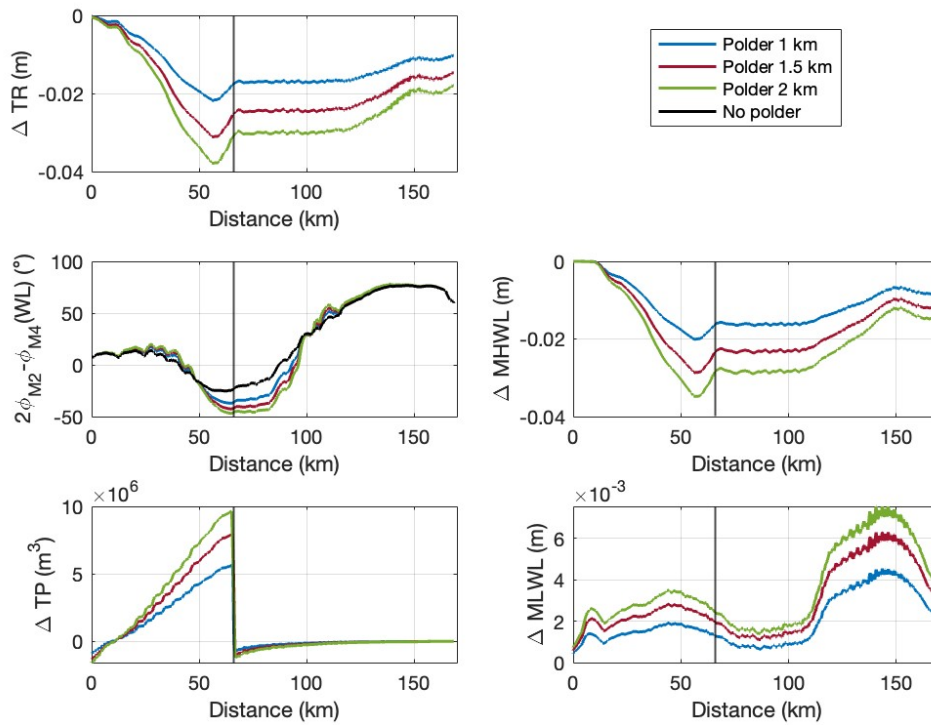
Figure 4.13: An overview of the change in tidal range (TR) along the channel for the three scenarios with different widths. Underneath, the phase difference between the M_2 and M_4 tidal constituents per model run are shown along the channel, calculated using water level data (WL). Underneath the change in flood tidal prism (TP) is shown. On the right, the change in mean high water level (MHWL) along the channel and mean low water level (MLWL) between the run without extra tidal area and with is shown. The vertical line shows the locations of the intertidal areas.

Along the entire channel, ebb velocity increases because of the implementation of the intertidal area. Before the intertidal area, the largest increase in ebb velocity was up to 0.03 m/s for the polder of 2 km wide. Furthermore, the change in velocity along the channel during ebb is greater if the shape of the intertidal area is wider. When examining the flood velocity profile along the channel, an even larger increase is visible just before the intertidal area, which is a maximum of 0.04 m/s. This increase is also larger for a wider intertidal area. After the water passes the intertidal area, the flood velocity decreases, which is greatest for the intertidal area with a width of 2 km and smallest for the intertidal area with a 1 km width (Figure 4.14). The friction in the channel shows a similar pattern to the flood velocity, which is the main cause of the increased friction in this system (Figure C.3 in the appendix).
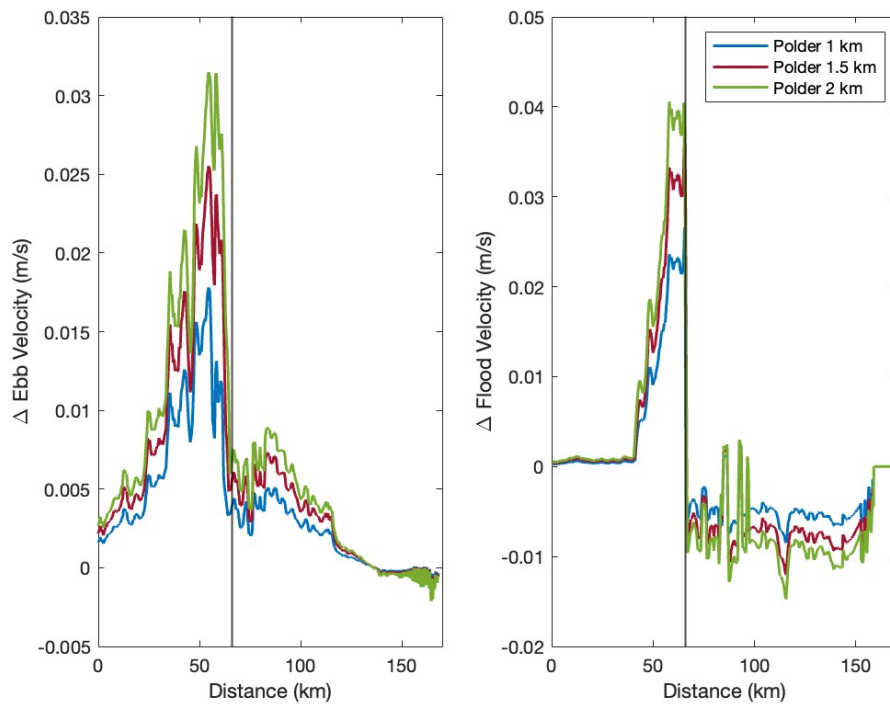
Figure 4.14: Change in ebb and flood velocity for an intertidal area of 3000 ha at 66 km with different shapes. The vertical black line shows the location of the intertidal area.

The energy balance along the entire channel decreases after the extra intertidal area is implemented. The decrease is greatest over the range of 50 kilometers landward of the location where the intertidal area is incorporated. The decrease is greater along the entire channel when an intertidal area that is wider (wider parallel to the channel) and stretches less far inland is implemented. For the kinetic energy part of the energy balance, a significant increase in kinetic energy before the intertidal area is visible again and a small decrease after, which is greater if the polder is wider. This pattern corresponds to the pattern visible in the flood velocity (Figure 4.14). The potential energy decreases along the entire channel and decreases most 8 kilometers before the intertidal area at the same location where the kinetic energy increases the most. Because the order of magnitude of the decrease in potential energy is greater than that of kinetic energy, the total energy still decreases along the channel but less at the location where the kinetic energy increase is greatest, and the tidal range also shows the greatest decrease at this location (Figure 4.15).

The change in tidal energy flux averaged over a single tidal cycle for a system with an intertidal area minus the tidal energy flux for the model run without a polder shows an increased change in energy flux seaward of the intertidal area. It is greater when the width of the area increases. Landward of the intertidal area, the energy flux decreases. No clear signs of tidal wave reflection are visible when studying the energy flux of the system (Figure 4.15).
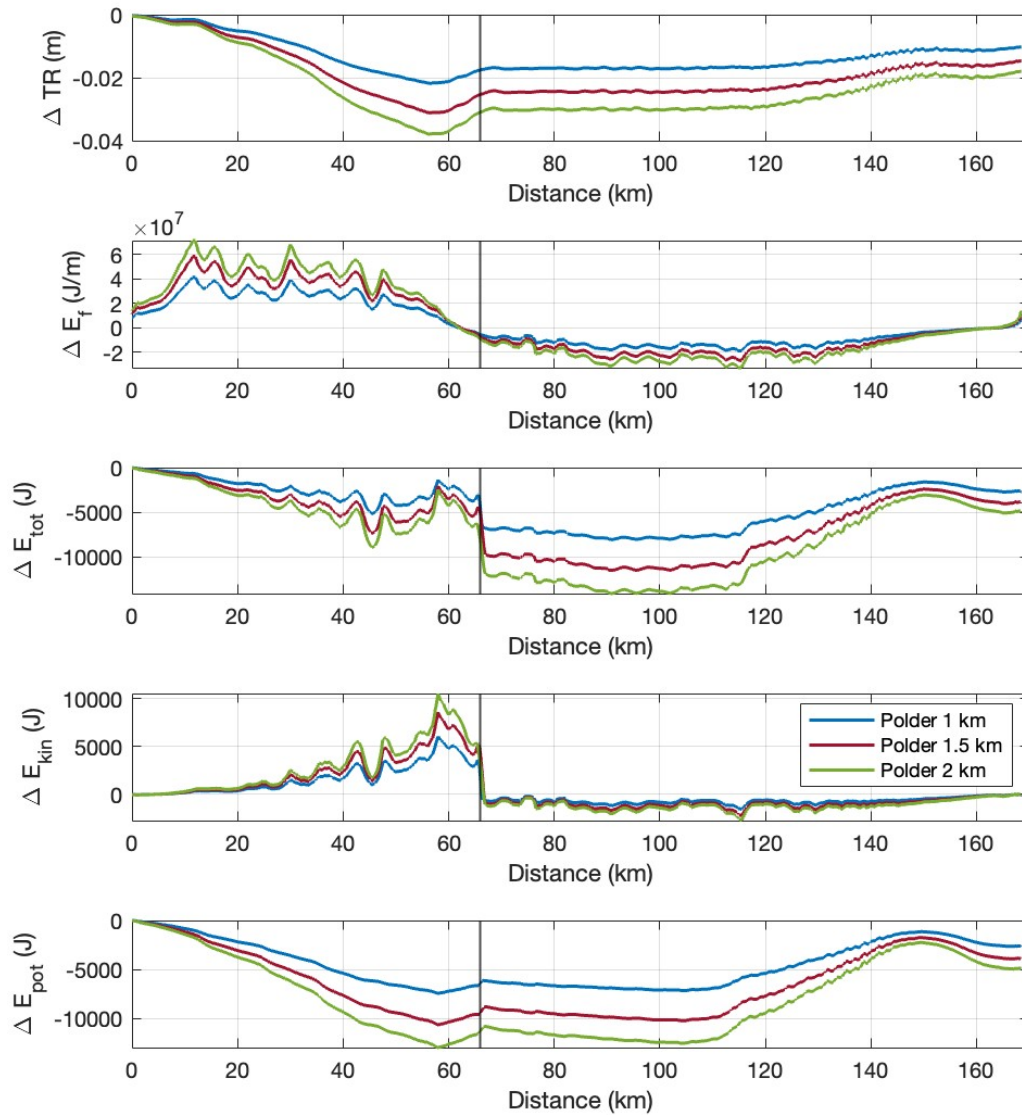
Figure 4.15: Change in tidal range (TR), change in tidal energy flux averaged over a single tidal cycle over the cross-section (E_f), total (E_{tot}), kinetic (E_{kin}), and potential (E_{pot}) tidal energy along the channel averaged over a single tidal cycle. The vertical black line shows the locations of the intertidal areas implemented in the different model runs.

5 | Discussion

To summarize the main findings of this study, the model study shows that the most important mechanism that influenced tidal hydrodynamics after wetland restoration was the increased storage area during high water due to the implementation of an intertidal area. This resulted in a water level gradient along the channel towards the location of the polder. Because of this water level gradient, there is an increased flow velocity in the channel seaward of the polder compared to the situation without the polder (Figure 5.1). The MHWL shows a sharp decrease before the polder, more than can be attributed to the increased storage capacity alone. Also, if that was the case, it was expected at the location of the polder and not before. A possible explanation is the Bernoulli effect, as the pressure (P) stays the same, but velocity (v) increases, so MHWL (h) should go down (see Equation 5.1) (Qin and Duan, 2017).

$$P + \frac{1}{2}\rho v^2 + \rho g h = constant \tag{5.1}$$

Additionally, because of the increased velocity in the channel seaward of the polder, the friction also increased and slowed the water movement, resulting in a decreased tidal range seaward of the intertidal area (see the cross-sections in Figure 5.1b, the tidal range follows the same line as the MHWL). The tidal prism increased near the intertidal area because of the increased storage capacity, indicating greater water exchange at this location in the system. Further seaward of the polder, the tidal prism decreases and becomes negative at the mouth. This can be explained by the decrease in tidal range, which means less water can be transported into the estuary at the river mouth, resulting in a decrease in tidal prism near the mouth for an intertidal area located further landward (Figure 5.1b). When a polder is implemented close to the river mouth, an increase in the tidal prism is visible at the mouth as more water can be pulled into the estuary because of the increased storage capacity.

Adding extra intertidal areas resulted in an overall decrease in tidal energy along the channel, which is the greatest landward of the intertidal area; further analysis of the tidal energy flux did not indicate that reflection of the tidal wave occurred because of the creation of additional intertidal area. An increase in ebb dominance is visible near the polder because water can flow into the intertidal area during high tide, decreasing the propagation speed during flood. This deceleration of water does not occur during ebb, as water cannot enter the intertidal area, resulting in the observed ebb dominance. However, less ebb-dominance is visible if the intertidal area is located at an elevation where water can enter the polder during ebb (at -2 m).

Generally, the main factors in the morphology of added wetlands that contribute to greater change in tidal hydrodynamics were the increase in width (parallel to the channel), the decrease in elevation, and a further distance from the river mouth. The increased width of the polder increased the distance along the channel over which the water could flow into the polder, creating a larger water level gradient along a larger transect, resulting in greater change in tidal hydrodynamics. The decrease in elevation resulted in a larger added storage volume, which affected the tidal hydrodynamics more. The greater effect of a polder located further landward was due to the relatively greater addition of storage volume compared to the local tidal prism, which decreased further landward due to the convergence of the channel.

The extensive data analysis of water level and velocity data gathered for the year before the opening of the Hedwige-Prosperpolder and the year after shows no significant changes in tidal range, MHWL, MLWL, and vertical tidal asymmetry, especially when compared to changes in these parameters for 2010-2020. The system was flood-dominated before the opening of the polder and continues to be so after the opening. It also shows differences for high and low water phase differences of only 1 to 2 minutes. These results found in the field measurements do not correspond to the predicted changes found after wetland restoration by the 2D model study from Stark et al. (2017).

Stark et al. (2017) suggests that the direction and magnitude of tidal asymmetry are affected after wetland restoration. Their study predicts that for an intertidal area of 1400 ha at 66 km from the mouth, there is a decrease in tidal range and MHWL of around 25 cm before the intertidal area. It also shows a reduction of flood dominance landward of the intertidal area and an increase in flood dominance seaward. The phase difference of high water increased up to 20 minutes before the implemented intertidal area. However, no changes of that magnitude were
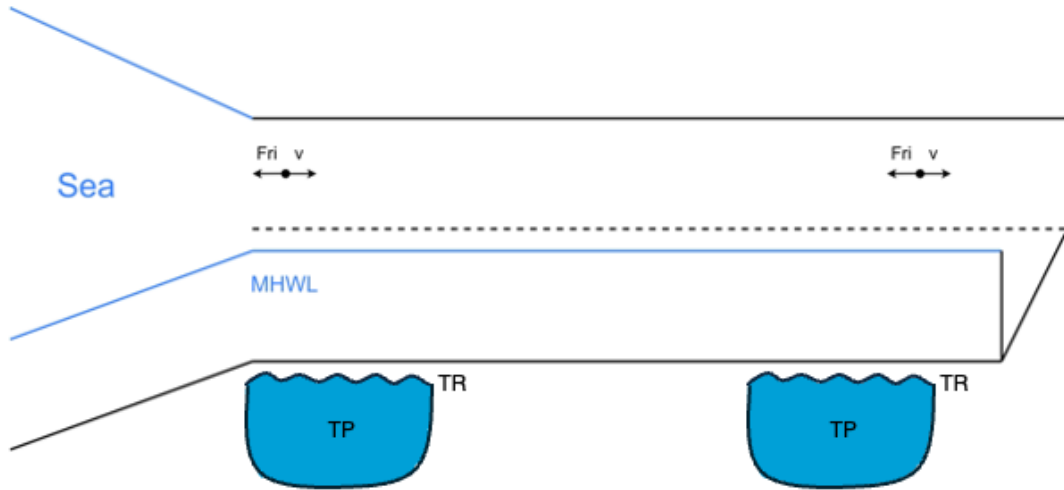
(a) Conceptual figure that describes the situation before adding extra intertidal area.
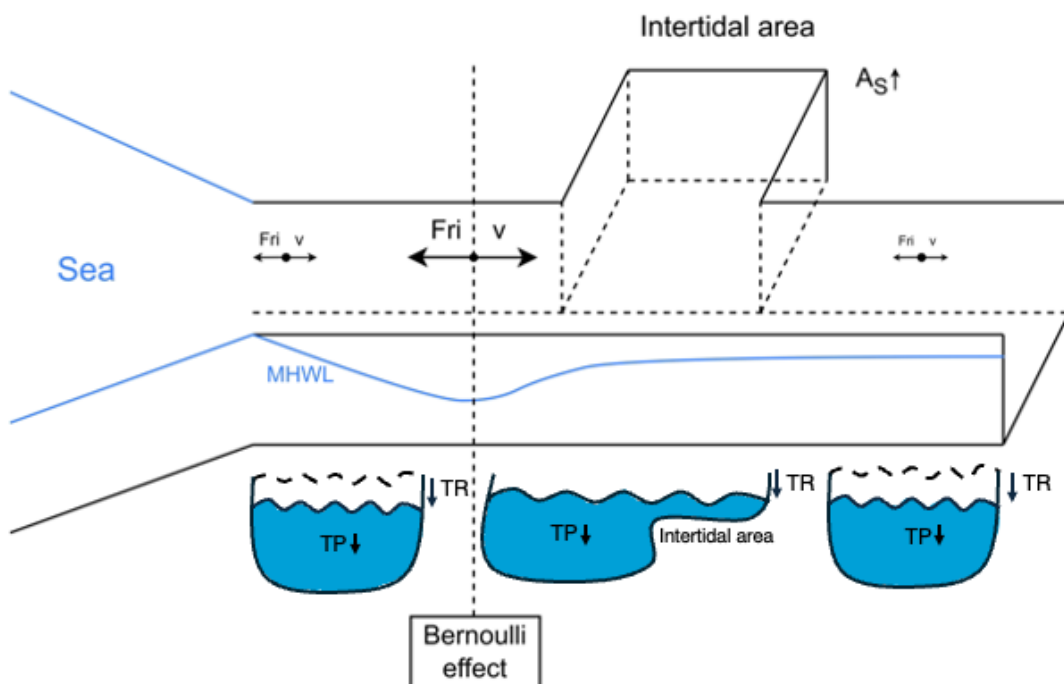
(b) Conceptual figure of the processes taking place after the implementation of the intertidal area.

Figure 5.1: Conceptual overview of the processes taking place after the addition of intertidal area far away from the river mouth. TP stands for tidal prism, TR equals tidal range, Fri is the friction, v is the velocity in the channel, MHWL is the mean high water level that changes along the channel, and As is the storage area. Underneath the river channel, three cross-sections are shown, of which the first shows the situation at the river mouth, the second at the location of the polder, and the third just landward of the polder.

observed for the Hedwige-Prosperpolder (located at 66 km with a size of 465 ha). The tidal range increased by 1 cm before the polder, a little less for MHWL, and the high water phase difference only increased by a maximum of 2 minutes. Also, no significant changes occurred in the measured average ebb and flood velocities.

A possible explanation for the fact that no changes in tidal hydrodynamics were measured in the field after the opening of the Hedwige-Prosperpolder, whereas several model studies (Talke and Jay, 2020; Stark et al., 2017; Weisscher et al., 2022) suggest that changes should occur, could be the size of the polder as the reclaimed wetland is only 465 ha compared to the intertidal areas of 1500 ha used in the model study. Furthermore, the signal that might exist due to the opening of the polder could be masked by other tidal and subtidal variations.

Due to the absence of significant changes in tidal hydrodynamics in the field measurements after the opening of the Hedwige-Prosperpolder, a 1D numerical model was used to investigate which morphological changes in tidal flats had more effect on tidal hydrodynamics and what process was the most important cause for the observed changes. The method to investigate this used by Stark et al. (2017) was a numerical 2D depth-averaged model of the Scheldt using the shallow water equations and a dimensionless friction coefficient that depends on the water level. The downstream boundary was forced by observed water levels from tidal stations near the river mouth, and the river discharge forced the upstream boundary. For this investigation, a 1D model was used containing the one-dimensional shallow water equations and a constant Chézy value for the channels. The river discharge also forced the upstream boundary. For the downstream boundary, a tidal signal consisting of only an M2, M4, and M6 tidal wave was imposed. Overall, the 1D model used in this thesis was a simplification of the model used by Stark et al. (2017), which is not able to capture the frictional effects of the intertidal areas but can still be used to study the along channel variation in tidal hydrodynamics.

This thesis used intertidal areas of twice the size used by Stark et al. (2017) at the same locations along the channel. I found similar patterns when adding intertidal areas at different locations along the channel for tidal range, tidal prism, MHWL, MLWL, and velocities, with a greater change for intertidal areas located further landward. However, effects on the tidal range, tidal prism, MHWL, MLWL, and velocities were much smaller; the tidal range was found to be half the size predicted by Stark et al. (2017), and velocities were up to an order of 10 smaller. This might suggest that the effect of wetland restoration is less pronounced than described by Stark et al. (2017). In their research, Stark et al. (2017) found a clear increase in flood dominance in the vertical tidal asymmetry seaward of the intertidal area. On the other hand, increased ebb dominance was found in the results of this 1D numerical model. A possible explanation for this discrepancy could be that in the 1D model, frictional effects within the intertidal area are not included, whereas these are considered in the study by Stark et al. (2017). Stark et al. (2017) shows that a reduction of the propagation speed of low water for tidal flats at a low elevation occurs, slowing down low water more than high water due to a larger water depth during high tide.

Stark et al. (2017) also looked into the effect of different elevations of intertidal flats within the channel on the tidal range and tidal prism. They found that for the lower part of the estuary, tidal flats with a low elevation of -2 m result in the greatest decrease in tidal range. However, tidal flats with a high elevation of +2 m result in the smallest decrease in tidal range. They found it was the other way around for intertidal areas further than 50 km from the river mouth. This study investigated the effect of tidal elevation for adjacent intertidal areas. However, these areas are not part of the flow-carrying capacity and generate slightly different results. Adding an intertidal area at 66 km decreased the tidal range the most for intertidal areas of -2m. Both studies found an increased tidal prism for scenarios with lower flats, and the peak flood velocity for both studies was highest for an elevation of -2 m. As for tidal asymmetry, Stark et al. (2017) found enhanced ebb-dominance for elevations of 0 and +1 m and enhanced flood dominance for elevations of -2m and -1 m because they are part of the flow-carrying cross-section. For this study, a decrease in ebb-dominance is found for most elevations except -2 m as dispersion of the water over the tidal flats during flood slows down the high water propagation more because low water cannot enter the tidal flats and is therefore not experiencing extra friction from the flats.

Other research from Weisscher et al. (2022) also showed that the effect of the opening of a polder further landward is greater than for a polder located closer to the river mouth, as was found in this thesis. Furthermore, they found that widening the inlet for the polder reduced the tidal range. However, no change in tidal prism was observed. This thesis found a decrease in the tidal range for a wider polder along the channel and a larger local

increase in the tidal prism for different polder widths along the channel. This difference might occur because no long-term morphological changes were built into the 1D model, as this thesis study focused only on the short-term effect of wetland restoration. For example, the rise of the intertidal area due to the import of sediments over a longer timescale was not taken into account, which was accounted for in the case for the study by Weisscher et al. (2022) and could lead to different conclusions.

It is important to understand the processes involved in wetland restoration and the consequences of those projects, as they are considered nature-based solutions to protect low-lying areas behind the dikes. The tidal flats have the potential to decrease flooding under storm conditions by the dissipation of wave and surge energy across the area. These measures are generally considered cheaper than hard coastal defense structures and are better for nature as well (Pontee et al., 2016). The decrease in tidal range seaward of implemented tidal areas found in this investigation and the decrease in tidal prism at the mouth are promising results to consider creating extra intertidal areas for flood protection in the future, especially because of mean sea level rise due to climate change. However, the changes in tidal range and tidal prism found in this study are only a few centimeters. Therefore, further research should also be done to further consider the damping effect of tidal flats on storm surges like the research from Smolders et al. (2015) and investigate their usefulness as a nature-based solution. Furthermore, the opening of the Hedwige-Prosperpolder did not show any significant changes in tidal hydrodynamics in the field. Therefore, it is recommended that changes in tidal hydrodynamics be investigated with field data for larger wetland restoration projects of different sizes for different estuarine systems to further investigate their suitability as a nature-based solution.

A limitation of the data analysis was that the tidal dynamics were calculated using T-tide, which does not account for a varying upstream river discharge. However, analysis of the Scheldt water level data in 2022 and 2023 showed the influence of river discharge on water levels in part of the upstream channel after large precipitation events. To simplify the analysis, and because only a small part of the upstream channel was influenced, T-tide was still used for the data analysis and was assumed to sufficiently predict the tides for the purpose of this study (Pawlowicz et al., 2002).

Furthermore, limitations of the numerical model were recognized. For the model, a wave consisting of tidal constituents M_2, M_4, and M_6 was imposed at the river mouth. Still, other constituents that occur in reality in the Scheldt were not taken into account, which could cause some discrepancy in the wave propagation and asymmetry compared to the real-life situation. Also, a constant upstream river discharge of 110 m^3/s and one constant Chézy coefficient for both the channel and intertidal area were assumed for the model, which does not exactly correspond to reality. But this should not influence the outcomes of this study too much as only changes in hydrodynamics along the channel were investigated, and the variety in the discharge of the river Scheldt is quite small, varying in the range of 50 to 200 m3/s (Van Rijn et al., 2010). Also, using these simplifications of reality made the interpretation of the model output easier and was sufficient as this study focused on large-scale along-channel changes in tidal hydrodynamics. Moreover, post-research, an error was discovered in the model concerning the accurate representation of the lateral term ($\frac{Q}{A_c}q_s$) within the momentum equation (Equation 3.5) when a polder is implemented. However, the size of the change in lateral flux because of the implementation of the polder is generally of the order of magnitude of 0.3 m^3/s^2 for a polder of 3000 ha. Therefore, the incorrect incorporation of this process most likely does not significantly change this study's outcomes. However, this discrepancy should be solved before further use of this numerical model.

In addition, a possible negative side effect of creating new tidal flats could be changed groundwater flows underneath the tidal flats. Because the dikes will be moved further inland, closer to the urban areas, the Scheldt will also flow closer to the villages, which can result in saline upward seepage in populated areas. Before considering more projects like the opening of the Hedwige-Prosperpolder, the scale of this possible negative effect should be considered. Another limitation of this study was that only the changes in tidal hydrodynamics on shorter timescales were taken into account, and no morphological feedbacks between the changed hydrodynamics and sediment transport were taken into account on longer timescales. Previous research from van Maren et al. (2023) stated that the response time of a system to interventions depends on the process driving the change, the system size, and the magnitude of the intervention. Additionally, Weisscher et al. (2022) found that opening a polder further landward causes the shallowing of the main channels in the long term because of increased flood dominance, influencing the hydrodynamics. To better understand the effects of large-scale changed morphology on tidal hydrodynamics after wetland restoration,

and the time it takes for the system to reach a new balance, further investigation is justified.

6 | Conclusion

This study investigated the process that explains the changes in tidal hydrodynamics of the Western Scheldt after wetland restoration. The most important process after adding the extra intertidal area is the establishment of the water level gradient along the channel towards the intertidal area. Because of this gradient, the velocity before the intertidal area in the channel is enhanced, which, as a result, decreases the MHWL because of the Bernoulli effect. Due to the increase in velocity, the friction also increases before the intertidal area in the channel, which decreases the tidal range as the movement of low to high tide and from high to low tide is slowed. The tidal prism also increases near the polder, indicating greater water exchange at this location in the system. Because of the decrease in tidal range, less water is transported into the estuary at the river mouth, resulting in a decrease in tidal prism near the mouth for polders located further landward. If a polder is added close to the mouth, the extra storage volume pulls more water into the estuary, increasing the tidal prism at the mouth.

Additionally, adding wetlands to the Scheldt results in additional tidal energy dissipation along the channel, which is the greatest landward of the intertidal area. No indication of tidal wave reflection was found using the energy flux after adding the intertidal area. For the tidal asymmetry, enhanced ebb-dominance occurs at the location of the intertidal area because the high water propagation slows down during flood as it enters the wetland, whereas, during low tide, the water cannot enter the polder and is therefore not slowed down.

Moreover, data analysis of water levels and velocities for the year before and after the opening of the Hedwige-Prosperpolder was performed. The analysis showed no significant changes in tidal hydrodynamics on the time scales considered in this study that were previously predicted by Weisscher et al. (2022); Stark et al. (2017). Probably because the restored wetland was one-third of the size of the wetlands used in the model study, and the signal that might exist due to the opening of the polder could be masked by other tidal and subtidal variations (Figure 4.4).

Since no significant changes in tidal hydrodynamics could be measured in the field, a 1D model was used to investigate what happens for wetland restoration projects larger than the Hedwige-Prosperpolder. These simulations for intertidal areas at different locations showed the same pattern as was found in the research by Stark et al. (2017), but the effects were overall smaller, suggesting that effects on the tidal asymmetry, tidal range, tidal prism, velocity, MHWL, and MLWL might be less pronounced than described in previous research.

Effects on tidal hydrodynamics of different elevations of adjacent intertidal areas and a wider polder parallel to the channel were not previously investigated. I found a decrease in the tidal range for a wider polder along the channel, a larger local increase in the tidal prism for increased polder widths, enhanced ebb-dominance, and more tidal energy dissipation along the entire channel. For the elevations varying between -2 and +2 m, the greatest changes in velocity, tidal range, tidal prism, and energy dissipation were shown for an elevation of -2 m, as the storage volume of this intertidal area was greatest. Only for the elevation of -2 m did the ebb-dominance of the vertical tidal asymmetry decrease as water could also enter the wetland during lower water levels, which decreased their propagation speed.

Overall, the morphological factors of intertidal areas that influenced the tidal hydrodynamics most were a wider (increasing width parallel to the channel) and deeper intertidal area of significant magnitude located further away from the river mouth. A location further inland was preferred as the relative contribution of the extra storage volume is greater compared to the local tidal prism upstream because of the channel's convergence. The decrease in elevation resulted in a larger added storage volume, which affected the tidal hydrodynamics more, and the increased width of the polder increased the distance along the channel over which the water could flow into the polder, creating a water level gradient along a larger transect, resulting in a greater change in tidal hydrodynamics.

Acknowledgements

Bibliography

Ahn, 2023. AHN Viewer. URL: https://www.ahn.nl/ahn-viewer.

Battjes, J.A., Labeur, R.J., 2017. Unsteady flow in open channels. Cambridge University Press.

Bilskie, M., Hagen, S., Medeiros, S., Passeri, D., 2014. Dynamics of sea level rise and coastal flooding on a changing landscape. Geophysical Research Letters 41, 927–934.

Blott, S.J., Pye, K., Van der Wal, D., Neal, A., 2006. Long-term morphological change and its causes in the mersey estuary, nw england. Geomorphology 81, 185–206.

Bolle, A., Wang, Z.B., Amos, C., De Ronde, J., 2010. The influence of changes in tidal asymmetry on residual sediment transport in the western scheldt. Continental Shelf Research 30, 871–882.

Claessens, J., van Openbare Werken, M., Zeediensten, A., . Het getij in de schelde. Stagevers lag van het Openbaar Ambt. Algemene directie van se lectie en vorming .

Coen, L., Peeters, P., Mostaert, F., 2008. Inventarisatie en historische analyse zeeschelde habitats: Effect antropogene ingrepen en natuurlijke evoluties op de getij-indringing in de zeeschelde-ondersteunende numerieke 1d-modellering. WL Rapporten .

Courant, R., Friedrichs, K., Lewy, H., 1967. On the partial difference equations of mathematical physics. IBM journal of Research and Development 11, 215–234.

Dauwe, W., 2019. Hedwige-prosperproject. URL: https://climate-adapt.eea.europa.eu/en/meta data/case-studies/a-transboundary-depolder ed-area-for-flood-protection-and-nature-hedwige-and-prosper-polders/hedwige-and- prosper-polders_document_brochure.pdf.

De Gelder, A., Techniek, C., Svaëek, I., 1996. Morfologie en modellering van de westerschelde .

Dronkers, J., 1986. Tidal asymmetry and estuarine morphology. Netherlands Journal of Sea Research 20, 117–131.

Dronkers, J.J., 1964. Tidal computations in rivers and coastal waters .

Edmonds, D., Caldwell, R., Baumgardner, S., Paola, C., Roy, S., Nelson, A., Nienhuis, J., 2017. A global analysis of human habitation on river deltas , 10832.

Friedrichs, C.T., Aubrey, D.G., 1988. Non-linear tidal distortion in shallow well-mixed estuaries: a synthesis. Estuarine, Coastal and Shelf Science 27, 521–545.

Friedrichs, C.T., Aubrey, D.G., 1994. Tidal propagation in strongly convergent channels. Journal of Geophysical Research: Oceans 99, 3321–3336.

Giese, B., Jay, D., 1989. Modelling tidal energetics of the columbia river estuary. Estuarine, Coastal and Shelf Science 29, 549–571.

Giosan, L., Syvitski, J., Constantinescu, S., Day, J., 2014. Climate change: Protect the world's deltas. Nature 516, 31–33.

Guo, L., Wang, Z.B., Townend, I., He, Q., 2019. Quantification of tidal asymmetry and its nonstationary variations. Journal of Geophysical Research: Oceans 124, 773–787.

Hoitink, A.J., Nittrouer, J.A., Passalacqua, P., Shaw, J.B., Langendoen, E.J., Huismans, Y., van Maren, D.S., 2020. Resilience of river deltas in the anthropocene. Journal of Geophysical Research: Earth Surface 125, e2019JF005201.

Jay, D.A., Giese, B.S., Sherwood, C.R., 1990. Energetics and sedimentary processes in the columbia river estuary. Progress in oceanography 25, 157–174.

Keith, D.A., Ferrer-Paris, J.R., Nicholson, E., Kingsford, R.T., 2020. Iucn global ecosystem typology 2.0. Descriptive profiles for biomes and ecosystem functional groups. IUCN, Gland .

Lin, N., Emanuel, K., Oppenheimer, M., Vanmarcke, E., 2012. Physically based assessment of hurricane surge threat under climate change. Nature Climate Change 2, 462–467.

Loucks, D.P., 2019. Developed river deltas: are they sustainable? Environmental Research Letters 14, 113004.

van Maren, D., Colina Alonso, A., Engels, A., Vandenbruwaene, W., de Vet, P., Vroom, J., Wang, Z., 2023. Adaptation timescales of estuarine systems to human interventions. Frontiers in earth science 11, 1111530.

Meire, P., Ysebaert, T., Damme, S.V., Bergh, E.V.d., Maris, T., Struyf, E., 2005. The scheldt estuary: a description of a changing ecosystem. Hydrobiologia 540, 1–11.

Neumann, B., Vafeidis, A.T., Zimmermann, J., Nicholls, R.J., 2015. Future coastal population growth and exposure to sea-level rise and coastal flooding-a global assessment. PloS one 10, e0118571.

NOS, 2022, June 7. Kabinet beslist deze maand over onder water zetten hedwigepolder. NOS URL: `https://nos.nl/artikel/2431756-kabinet-besl ist-deze-maand-over-onder-water-zetten-hedw igepolder`.

NOS, 2022a, October 25. Eerste water stroomt zeeuwse hedwigepolder binnen. NOS URL: `https://nos.nl/artikel/2449770-eerste-water -stroomt-zeeuwse-hedwigepolder-binnen`.

Nunn, P.D., Veitayaki, J., Ram-Bidesi, V., Vunisea, A., 1999. Coastal issues for oceanic islands: implications for human futures, in: Natural Resources Forum, Wiley Online Library. pp. 195–207.

Oppenheimer, M., Glavovic, B., Hinkel, J., van de Wal, R., Magnan, A., Abd-Elgawad, A., Cai, R., Cifuentes-Jara, M., DeConto, R., Ghosh, T., Hay, J., Isla, F., Marzeion, B., Meyssignac, B., Sebesvari, Z., 2019. Sea level rise and implications for low-lying islands, coasts and communities. IPCC Special Report on the Ocean and Cryosphere in a Changing Climate .

Parker, B.B., 1984. Frictional effects on the tidal dynamics of a shallow estuary (compound, surge-tide, river-tide interaction). The Johns Hopkins University.

Parker, B.B., 2007. Tidal analysis and prediction .

Pawlowicz, R., Beardsley, B., Lentz, S., 2002. Classical tidal harmonic analysis including error estimates in matlab using t_tide. Computers & Geosciences 28, 929–937.

Pontee, N., Narayan, S., Beck, M.W., Hosking, A.H., 2016. Nature-based solutions: lessons from around the world, in: Proceedings of the Institution of Civil Engineers-Maritime Engineering, Thomas Telford Ltd. pp. 29–36.

Qin, R., Duan, C., 2017. The principle and applications of bernoulli equation, in: Journal of Physics: Conference Series, IOP Publishing. p. 012038.

Rijkswaterstaat, n.d. Rijkswaterstaat waterinfo URL: `https://waterinfo.rws.nl//nav/index`. accessed: October 17, 2023.

van Rijn, L.C., 2011. Analytical and numerical analysis of tides and salinities in estuaries; part i: tidal wave propagation in convergent estuaries. Ocean dynamics 61, 1719–1741.

Scheyen, J.D., 2023, 25 mei. Prijsvraag nieuwe naam hedwigepolder gestopt na ophef. RD.nl. URL: `https://www.rd.nl/artikel/1021412-prijsvraag -nieuwe-naam-hedwigepolder-gestopt-na-ophef`.

Smolders, S., Plancke, Y., Ides, S., Meire, P., Temmerman, S., 2015. Role of intertidal wetlands for tidal and storm tide attenuation along a confined estuary: a model study. Natural Hazards and Earth System Sciences 15, 1659–1675.

Song, D., Wang, X.H., Zhu, X., Bao, X., 2013. Modeling studies of the far-field effects of tidal flat reclamation on tidal dynamics in the east china seas. Estuarine, Coastal and Shelf Science 133, 147–160.

Speer, P., Aubrey, D., 1985. A study of non-linear tidal propagation in shallow inlet/estuarine systems part ii: Theory. Estuarine, Coastal and Shelf Science 21, 207–224.

Van der Spek, A., 1997. Tidal asymmetry and long-term evolution of holocene tidal basins in the netherlands: simulation of palaeo-tides in the schelde estuary. Marine geology 141, 71–90.

Stark, J., Smolders, S., Meire, P., Temmerman, S., 2017. Impact of intertidal area characteristics on estuarine tidal hydrodynamics: A modelling study for the scheldt estuary. Estuarine, Coastal and Shelf Science 198, 138–155.

Talke, S.A., Jay, D.A., 2020. Changing tides: The role of natural and anthropogenic factors. Annual review of marine science 12, 121–151.

Temmerman, S., Horstman, E.M., Krauss, K.W., Mullarney, J.C., Pelckmans, I., Schoutens, K., 2023. Marshes and mangroves as nature-based coastal storm buffers. Annual Review of Marine Science 15, 95–118.

Van Rijn, L., et al., 2010. Tidal phenomena in the scheldt estuary. Report, Deltares 105, 99.

Wang, Z.B., Jeuken, C., De Vriend, H., 1999. Tidal asymmetry and residual sediment transport in estuaries. Technical Report. Deltares (WL).

Wang, Z.B., Jeuken, M., Gerritsen, H., De Vriend, H., Kornman, B., 2002. Morphology and asymmetry of the vertical tide in the westerschelde estuary. Continental Shelf Research 22, 2599–2609.

Waterinfo, n.d. Waterinfo vlaanderen. URL: `https://www.waterinfo.be/`. accessed: March 13, 2024.

van Infrastructuur en Waterstaat, M., 2022, 27 december. Westerschelde - informatie en waterdata URL: `https://www.rijkswaterstaat.nl/water/vaar wegenoverzicht/westerschelde`.

Wei, X., Cai, S., Zhan, W., 2021. Impact of anthropogenic activities on morphological and deposition flux changes in the pearl river estuary, china. Scientific Reports 11, 16643.

Weisscher, S.A., Baar, A.W., Van Belzen, J., Bouma, T.J., Kleinhans, M.G., 2022. Transitional polders along estuaries: Driving land-level rise and reducing flood propagation. Nature-Based Solutions 2, 100022.

Zeeuws Landschap, H., n.d. Geschiedenis van saeftinghe | verdronken land van saeftinghe. URL: `https://www.hetzeeuwselandschap.nl/natuurgebieden/verdronken land-van-saeftinghe/geschiedenis-van-saeftinghe`.

A | Model calibration

C	RMSE TR	RMSE M2 amp	RMSE M2 pha	RMSE M4 amp	RMSE M4 pha
30 $m^{0.5}/s$	1.06 m	0.45 m	126 °	0.08 m	141 °
31 $m^{0.5}/s$	0.96 m	0.40 m	124 °	0.07 m	140 °
32 $m^{0.5}/s$	0.87 m	0.36 m	121 °	0.07 m	139 °
33 $m^{0.5}/s$	0.79 m	0.32 m	119 °	0.07 m	136 °
34 $m^{0.5}/s$	0.70 m	0.28 m	117 °	0.07 m	134 °
35 $m^{0.5}/s$	0.62 m	0.25 m	116 °	0.07 m	132 °
36 $m^{0.5}/s$	0.54 m	0.21 m	114 °	0.07 m	131 °
37 $m^{0.5}/s$	0.47 m	0.18 m	112 °	0.07 m	129 °
38 $m^{0.5}/s$	0.39 m	0.15 m	111 °	0.07 m	127 °
39 $m^{0.5}/s$	0.33 m	0.13 m	110 °	0.06 m	126 °
40 $m^{0.5}/s$	0.27 m	0.12 m	109 °	0.06 m	125 °
41 $m^{0.5}/s$	0.23 m	0.11 m	107 °	0.06 m	124 °
42 $m^{0.5}/s$	0.20 m	0.11 m	106 °	0.06 m	123 °
43 $m^{0.5}/s$	0.20 m	0.14 m	105 °	0.06 m	122 °
44 $m^{0.5}/s$	0.23 m	0.16 m	103 °	0.06 m	122 °
45 $m^{0.5}/s$	0.27 m	0.18 m	102 °	0.06 m	122 °
46 $m^{0.5}/s$	0.32 m	0.20 m	101 °	0.06 m	122 °
47 $m^{0.5}/s$	0.37 m	0.23 m	100 °	0.06 m	121 °
48 $m^{0.5}/s$	0.43 m	0.26 m	99 °	0.06 m	121 °
49 $m^{0.5}/s$	0.48 m	0.29 m	98 °	0.06 m	121 °
50 $m^{0.5}/s$	0.54 m	0.32 m	97 °	0.07 m	120 °
51 $m^{0.5}/s$	0.59 m	0.34 m	96 °	0.07 m	119 °
52 $m^{0.5}/s$	0.65 m	0.37 m	95 °	0.07 m	119 °
53 $m^{0.5}/s$	0.70 m	0.40 m	95 °	0.07 m	118 °
54 $m^{0.5}/s$	0.75 m	0.42 m	95 °	0.07 m	117 °
55 $m^{0.5}/s$	0.80 m	0.45 m	94 °	0.07 m	117 °
56 $m^{0.5}/s$	0.86 m	0.47 m	93 °	0.07 m	116 °
57 $m^{0.5}/s$	0.90 m	0.50 m	92 °	0.07 m	115 °
58 $m^{0.5}/s$	0.95 m	0.52 m	91 °	0.07 m	115 °
59 $m^{0.5}/s$	1.00 m	0.55 m	90 °	0.07 m	111 °
60 $m^{0.5}/s$	1.05 m	0.57 m	90 °	0.07 m	110 °
61 $m^{0.5}/s$	1.09 m	0.60 m	89 °	0.07 m	109 °
62 $m^{0.5}/s$	1.14 m	0.61 m	88 °	0.08 m	110 °
63 $m^{0.5}/s$	1.18 m	0.64 m	88 °	0.08 m	108 °
64 $m^{0.5}/s$	1.22 m	0.66 m	87 °	0.08 m	107 °
65 $m^{0.5}/s$	1.26 m	0.68 m	87 °	0.08 m	105 °
66 $m^{0.5}/s$	1.30 m	0.70 m	86 °	0.08 m	106 °
67 $m^{0.5}/s$	1.34 m	0.72 m	86 °	0.08 m	106 °
68 $m^{0.5}/s$	1.38 m	0.74 m	86 °	0.08 m	105 °
69 $m^{0.5}/s$	1.41 m	0.76 m	85 °	0.08 m	105 °
70 $m^{0.5}/s$	1.45 m	0.78 m	84 °	0.09 m	106 °
71 $m^{0.5}/s$	1.45 m	0.78 m	84 °	0.09 m	106 °

Table A.1: An overview of the root mean squared error (RMSE) for 42 model runs with a different Chézy coëfficient ranging between 30 and 70 $m^{0.5}/s$. The RMSE is calculated for the difference between the average measured value along the channel in the year 2021 and the results of the model along the channel. In this case, only the RMSE of the tidal range (TR), M2 amplitude, M2 phase, M4 amplitude, and M4 phase are considered.

Q	RMSE TR	RMSE M2 amp	RMSE M2 pha	RMSE M4 amp	RMSE M4 pha
90 m^3/s	0.244 m	0.108 m	105 °	0.066 m	136 °
91 m^3/s	0.244 m	0.108 m	105 °	0.066 m	136 °
92 m^3/s	0.243 m	0.107 m	105 °	0.066 m	136 °
93 m^3/s	0.242 m	0.107 m	105 °	0.066 m	136 °
94 m^3/s	0.241 m	0.106 m	105 °	0.066 m	136 °
95 m^3/s	0.241 m	0.105 m	105 °	0.066 m	136 °
96 m^3/s	0.240 m	0.105 m	105 °	0.066 m	136 °
97 m^3/s	0.240 m	0.104 m	105 °	0.066 m	137 °
98 m^3/s	0.239 m	0.104 m	105 °	0.066 m	137 °
99 m^3/s	0.238 m	0.103 m	105 °	0.066 m	137 °
100 m^3/s	0.238 m	0.103 m	105 °	0.066 m	137 °
101 m^3/s	0.237 m	0.102 m	105 °	0.066 m	137 °
102 m^3/s	0.237 m	0.102 m	105 °	0.066 m	137 °
103 m^3/s	0.237 m	0.101 m	105 °	0.066 m	137 °
104 m^3/s	0.237 m	0.101 m	105 °	0.066 m	137 °
105 m^3/s	0.236 m	0.101 m	105 °	0.066 m	137 °
106 m^3/s	0.236 m	0.100 m	105 °	0.066 m	137 °
107 m^3/s	0.236 m	0.099 m	105 °	0.066 m	137 °
108 m^3/s	0.236 m	0.099 m	105 °	0.066 m	137 °
109 m^3/s	0.236 m	0.099 m	105 °	0.066 m	137 °
110 m^3/s	0.236 m	0.098 m	105 °	0.066 m	137 °
111 m^3/s	0.236 m	0.098 m	105 °	0.066 m	137 °
112 m^3/s	0.236 m	0.098 m	105 °	0.065 m	137 °
113 m^3/s	0.236 m	0.098 m	105 °	0.065 m	137 °
114 m^3/s	0.236 m	0.097 m	105 °	0.065 m	137 °
115 m^3/s	0.237 m	0.098 m	105 °	0.065 m	137 °

Table A.2: Overview of the result of the different calibration runs with different upstream river discharges ranging between 90 and 115 m^3/s shown in the different rows. The different columns show from left to right the root mean squared error of the tidal range (TR), M2 amplitude, M2 phase, M4 amplitude, and M4 phase.

M2 amp	RMSE TR	RMSE M2 amp	RMSE M2 pha	RMSE M4 amp	RMSE M4 pha
1.55 m	0.52 m	0.15 m	11 °	0.08 m	89 °
1.60 m	0.44 m	0.16 m	12 °	0.08 m	89 °
1.65 m	0.38 m	0.13 m	14 °	0.08 m	90 °
1.70 m	0.30 m	0.11 m	14 °	0.08 m	91 °
1.75 m	0.24 m	0.09 m	15 °	0.08 m	93 °
1.80 m	0.21 m	0.09 m	15 °	0.08 m	92 °
1.85 m	0.20 m	0.10 m	16 °	0.08 m	90 °
1.90 m	0.23 m	0.12 m	17 °	0.07 m	90 °
1.95 m	0.28 m	0.15 m	17 °	0.07 m	90 °

Table A.3: An overview of the result of the different calibration runs with different M2 amplitudes for the downstream boundary condition ranging between 1.55 and 1.95 m in the different rows. The different columns show from left to right the root mean squared error of the tidal range (TR), M2 amplitude, M2 phase, M4 amplitude, and M4 phase.

Parameter name	Value	Explanation of parameter
tN	10*24*3600	Run time in seconds
N	tN/5	Number of run timesteps
Nout	tN/600	Number of output time steps
ω_{M_2}	$2\pi/(12.42*3600)$	Angular frequency of M_2 (rad/s)
H_{M_2}	1.85	Amplitude of M_2 (m)
H_{M_4}	0.14	Amplitude of M_4 (m)
H_{M_6}	0.0931	Amplitude of M_6 (m)
ϕ_{M_4}	-0.1333	Change in phase $2\phi_{M_2} - \phi_{M_4}$ (rad)
ϕ_{M6}	-1.3865	Change in phase $3\phi_{M_2} - \phi_{M_6}$ (rad)
M2_contribution	$H_{M_2} * cos(\omega_{M_2} * t)$	M_2 tidal wave equation
M4_contribution	$H_{M_4} * cos(2 * \omega_{M_2} * t - \phi_{M_4})$	M_4 tidal wave equation
M6_contribution	$H_{M_6} * cos(2 * \omega_{M_2} * t - \phi_{M_6})$	M_6 tidal wave equation
bc0_H	M2_contribution + M4_contribution + M6_contribution	Downstream boundary condition (Water level)
bcL_Q	-110	Upstream boundary condition (River discharge)
L	168500	Length channel
D50	2e-4	Sediment size
shieldscrit	0.145	Critical shield stress
C	42	Chézy constant
h0	Mean High Water Level from data analysis of 2021 along channel	Initial water level
Q0	-110	Initial discharge
geomtabs	*Tables with geometric data	Tables that contain bathymetric data from the Scheldt

Table A.4: An overview of all model input parameters used for the final model runs.

B | Data analysis for variation over multiple years

Years	WEST	VLI	TER	OVH	WAL	BAAL	BAT	LIEF	ANTW	HEM	TEM	SINT	DER	SCHO	WET	MEL
2010	-	-	-	-	-	-	-	-	-	-	-	-	-	-	-	-
2011	0.023	0.028	0.033	-0.006	0.041	0.044	0.046	0.008	0.014	0.074	0.087	0.056	0.079	0.071	0.082	0.099
2012	0	0	0.002	0.008	0.003	0.004	0.005	0.02	0.004	0.002	-0.024	-0.025	-0.037	-0.055	-0.075	-0.139
2013	0.018	0.02	0.022	0.035	0.019	0.02	0.02	0.048	0.031	-0.004	0.026	0.008	0.003	-0.03	-0.056	-0.129
2014	0.026	0.028	0.034	0.039	0.029	0.03	0.033	0.042	0.03	0.016	0.032	0.069	0.066	0.06	0.065	0.114
2015	0.022	0.017	0.01	-0.033	0.022	0.023	0.036	-0.048	-0.046	-0.052	-0.046	-0.049	-0.019	0.019	-0.018	0.017
2016	-0.016	-0.017	-0.012	-0.02	-0.016	-0.017	-0.017	-0.016	0.015	-0.02	0.011	-0.011	0.001	-0.042	-0.054	-0.063
2017	-0.01	-0.012	-0.014	-0.022	-0.018	-0.019	-0.02	-0.02	-0.041	-0.007	-0.022	0.035	0.07	0.079	0.058	0.137
2018	-0.013	-0.008	-0.016	0.029	-0.015	-0.016	-0.019	0.001	0.018	0.024	-0.013	-0.013	0.012	0.009	1.428	1.418
2019	-0.011	-0.021	-0.018	-0.055	-0.028	-0.03	-0.032	-0.063	-0.062	-0.075	-0.05	-0.025	-0.011	0.01	0.047	0.078
2020	-0.026	-0.027	-0.031	-0.01	-0.025	-0.026	-0.028	-0.028	-0.022	-0.022	-0.024	-0.024	-0.014	0	-0.028	-0.05
Max	0.026	0.028	0.034	0.055	0.041	0.044	0.046	0.063	0.062	0.075	0.087	0.069	0.079	0.079	1.428	1.418

Table B.1: Tidal range difference (m) between consecutive years per station. The bottom row contains the maximum difference between years per station. The time span considered is eleven years, starting from the first of January 2010 to the 31st of December 2020. An overview of the full station names, which are only visible in abbreviation here can be found in the Appendix but the stations are in order from the river mouth to Gent from left to right.

Years	WEST	VLI	TER	OVH	WAL	BAAL	BAT	LIEF	ANTW	HEM	TEM	SINT	DER	SCHO	WET	MEL
2010	-	-	-	-	-	-	-	-	-	-	-	-	-	-	-	-
2011	0.01	0.011	0.013	-0.003	0.014	0.012	0.012	-0.03	-0.008	-0.009	-0.001	0.002	-0.014	-0.047	-0.075	-0.081
2012	-0.002	-0.001	0	0.014	0.002	0.003	0.001	0.018	0.009	0.005	0.007	0.001	0.021	0.04	0.074	0.129
2013	0.005	0.005	0.003	-0.001	0.003	0.003	0.003	0.005	0	-0.014	-0.017	-0.001	0.013	0.017	0.042	0.063
2014	0.01	0.01	0.011	0.033	0.01	0.01	0.01	0.033	0.025	0.024	0.007	0.018	0	-0.026	-0.062	-0.097
2015	0.009	0.014	0.012	-0.015	0.006	0.005	0.009	-0.013	-0.026	-0.004	-0.018	-0.014	-0.014	-0.003	-0.025	-0.041
2016	-0.007	-0.008	-0.008	-0.014	-0.006	-0.004	-0.005	-0.006	0.017	-0.002	0.012	0.005	0.016	0.021	0.042	0.067
2017	-0.004	-0.005	-0.003	-0.009	-0.007	-0.006	-0.006	-0.007	-0.013	-0.008	-0.011	-0.009	-0.013	-0.041	-0.094	-0.122
2018	-0.001	-0.002	-0.002	0.006	-0.001	-0.002	-0.002	-0.006	-0.024	-0.006	-0.021	-0.015	-0.012	-0.002	0.129	0.154
2019	-0.006	-0.005	-0.008	0.004	-0.007	-0.007	-0.005	0.009	0.002	0.001	0.004	0.013	0.004	-0.001	-0.01	-0.036
2020	-0.01	-0.013	-0.011	0.004	-0.01	-0.009	-0.012	-0.007	0.007	0.004	0.005	0.023	0.02	0.037	0.064	0.088
Max	0.01	0.013	0.012	0.033	0.007	0.01	0.012	0.033	0.026	0.024	0.021	0.023	0.021	0.037	0.129	0.154

Table B.2: Mean high water level (MHWL) difference (m) between consecutive years per station. The bottom row contains the maximum difference between years per station. The time span considered is eleven years, starting from the first of January 2010 to the 31st of December 2020. An overview of the full station names, which are only visible in abbreviation here can be found in the Appendix but the stations are in order from the river mouth to Gent from left to right.

Years	WEST	VLI	TER	OVH	WAL	BAAL	BAT	LIEF	ANTW	HEM	TEM	SINT	DER	SCHO	WET	MEL
2010	-	-	-	-	-	-	-	-	-	-	-	-	-	-	-	-
2011	-0.004	-0.006	-0.005	-0.001	-0.006	-0.007	-0.007	-0.045	-0.02	-0.054	-0.03	-0.029	-0.047	-0.041	-0.046	-0.011
2012	0	0.001	0	0.005	0	0	-0.001	0.001	0.001	-0.004	0.013	0.006	0.025	0.034	0.03	0.032
2013	-0.003	-0.003	-0.004	-0.014	-0.004	-0.004	-0.004	-0.014	-0.009	-0.016	-0.027	-0.002	0.01	0.016	0.007	0.009
2014	-0.006	-0.006	-0.005	0.008	-0.006	-0.006	-0.006	0.01	0.013	0.011	-0.02	-0.006	-0.006	0.003	0.018	0.021
2015	-0.008	0	-0.009	0.013	-0.004	-0.003	-0.022	0.021	0.001	0.029	0.007	0.009	-0.019	-0.041	-0.04	-0.044
2016	0.003	0.004	0.002	-0.003	0.004	0.004	0.003	0.008	0.012	0.011	0.008	0.011	0.011	0.014	0.011	0.024
2017	0.003	0.002	0.003	0.014	0.002	0.003	0.002	0.011	0.014	0.002	0.003	-0.027	-0.038	-0.037	-0.019	-0.024
2018	0.001	0.002	0.002	-0.045	0.003	0.002	0.004	-0.025	-0.054	-0.035	-0.028	-0.02	-0.03	-0.021	-0.042	-0.004
2019	0.003	0.004	0.003	0.043	0.003	0.004	0.005	0.06	0.044	0.051	0.035	0.031	0.02	0.012	0.011	-0.01
2020	0.006	0.005	0.007	0.001	0.008	0.008	0.005	-0.012	0.001	0.003	0.005	0.026	0.006	0.003	0.014	0.008
Max	0.008	0.006	0.009	0.045	0.008	0.008	0.022	0.025	0.054	0.051	0.035	0.031	0.038	0.041	0.042	0.044

Table B.3: Mean low water level (MLWL) difference (m) between consecutive years per station (m). The bottom row contains the maximum difference between years per station. The time span considered is eleven years, starting from the first of January 2010 to the 31st of December 2020. An overview of the full station names, which are only visible in abbreviation here can be found in the Appendix but the stations are in order from the river mouth to Gent from left to right.

Years	WEST	VLI	TER	OVH	WAL	BAAL	BAT	LIEF	ANTW	HEM	TEM	SINT	DER	SCHO	WET	MEL
2010	-	-	-	-	-	-	-	-	-	-	-	-	-	-	-	-
2011	0	0.16	0.06	-3.08	-1.03	-0.57	-0.42	-10.24	-10.35	-10.55	-10.36	-10.44	-10.14	-10.07	-10.04	-10.25
2012	0	-0.12	-0.17	0.92	0.14	0.22	-0.22	0.15	0.29	0.40	-0.02	-0.35	-0.61	-1.10	-2.47	-4.43
2013	0	0.23	0.12	0.00	-0.53	-0.19	0.07	-2.08	-1.33	-2.44	-2.02	-0.27	-1.77	-2.35	-2.21	-2.57
2014	0	0.47	0.30	-1.30	0.41	0.53	0.46	-0.75	-1.21	-1.79	0.98	-0.87	-1.80	0.40	1.84	2.07
2015	0	-0.26	-2.11	1.02	0.31	-0.02	-0.03	1.52	1.89	1.14	1.29	1.37	1.62	1.45	1.83	5.27
2016	0	-0.21	0.43	0.01	0.03	-0.11	-0.13	1.30	0.79	1.47	1.17	1.02	1.23	-0.36	3.26	1.17
2017	0	0.47	-0.20	-1.21	0.01	0.09	-0.14	0.13	-0.03	0.07	0.18	-0.11	0.11	-0.07	2.04	2.96
2018	0	-0.27	0.10	-0.67	0.89	0.78	1.00	6.20	11.67	6.85	6.50	6.12	5.83	5.90	7.44	5.20
2019	0	0.07	0.11	-2.02	-1.20	-1.17	-1.21	-8.95	-14.31	-8.42	-9.40	-9.44	-8.77	-8.20	-7.78	-7.74
2020	0	-0.61	-0.88	-2.21	-1.05	-1.19	-0.94	-1.21	-1.36	-1.63	-1.73	-2.25	-2.19	-2.22	-4.73	-5.02
Max	*0*	*0.61*	*2.11*	*3.08*	*1.20*	*1.19*	*1.21*	*10.24*	*14.31*	*10.55*	*10.36*	*10.44*	*10.14*	*10.07*	*10.04*	*10.25*

Table B.4: Phase difference of high water (min) between consecutive years per station (m). The bottom row contains the maximum difference between years per station. The time span considered is eleven years, starting from the first of January 2010 to the 31st of December 2020. An overview of the full station names, which are only visible in abbreviation here can be found in the Appendix but the stations are in order from the river mouth to Gent from left to right.

Years	WEST	VLI	TER	OVH	WAL	BAAL	BAT	LIEF	ANTW	HEM	TEM	SINT	DER	SCHO	WET	MEL
2010	-	-	-	-	-	-	-	-	-	-	-	-	-	-	-	-
2011	0	-1.38	-2.32	1.74	0.19	0.54	0.59	0.95	0.91	0.72	0.41	1.08	0.68	1.16	-0.86	-3.16
2012	0	-0.31	-0.88	-1.06	-0.47	-1.01	-0.56	-0.47	-0.26	-0.04	-0.10	0.47	1.14	1.40	2.48	4.36
2013	0	0.06	0.02	-1.13	-0.55	-0.17	-0.87	-2.07	-2.00	-1.36	-3.29	-0.14	-0.67	-0.94	0.95	3.10
2014	0	0.57	2.61	2.15	0.19	1.09	2.86	5.55	-1.06	0.51	2.74	-0.17	-1.75	0.30	-0.75	-0.61
2015	0	0.00	-1.83	0.46	0.76	-0.11	-0.87	-1.65	4.24	3.35	0.15	1.82	2.60	0.00	-1.46	-2.71
2016	0	0.41	-0.55	0.31	-0.02	0.15	-0.04	1.03	1.12	1.03	1.07	1.31	1.68	1.73	2.22	2.38
2017	0	-0.39	-0.35	1.27	-0.66	-0.75	-1.09	-0.98	-1.11	-0.92	-1.09	-2.17	-2.76	-3.78	-5.21	-7.93
2018	0	-0.58	3.45	-1.86	-0.68	-1.11	-0.54	0.94	1.48	1.28	1.64	1.31	1.96	1.99	4.76	3.71
2019	0	0.33	-3.76	-0.92	1.26	1.34	0.63	-2.72	-3.21	-3.32	-3.60	-3.49	-4.09	-4.07	-5.17	-7.01
2020	0	0.01	-0.17	-1.63	-0.44	-0.17	0.04	-0.31	-0.09	0.02	0.23	-0.40	0.21	0.22	1.58	2.47
Max	*1.38*	*1.38*	*3.76*	*2.15*	*1.26*	*1.34*	*2.86*	*5.55*	*4.24*	*3.35*	*3.60*	*3.49*	*4.09*	*4.07*	*5.21*	*7.93*

Table B.5: Phase difference of low water (min) between consecutive years per station (m). The bottom row contains the maximum difference between years per station. The time span considered is eleven years, starting from the first of January 2010 to the 31st of December 2020. An overview of the full station names, which are only visible in abbreviation here can be found in the Appendix but the stations are in order from the river mouth to Gent from left to right.

	Mean V_{flood} (m/s)	Mean V_{ebb} (m/s)	ΔV_{flood} (%)	ΔV_{ebb} (%)
2010	0.801	-0.742	-	-
2011	0.676	-0.679	-15.61	-8.49
2012	0.757	-0.757	11.98	11.49
2013	0.481	-0.481	-36.46	-36.46
2014	0.783	-0.740	62.79	53.85
2015	0.738	-0.745	-5.75	0.68
2022	0.874	-0.992	-	-
2023	0.935	-1.046	6.98	5.44

Table B.6: The average maximum flood and ebb velocity for the point measurement station near Antwerp in m/s. ΔV_{flood} shows the percentual difference between the flood velocity in a certain year compared to the previous year. ΔV_{ebb} does the same but for the ebb velocity.
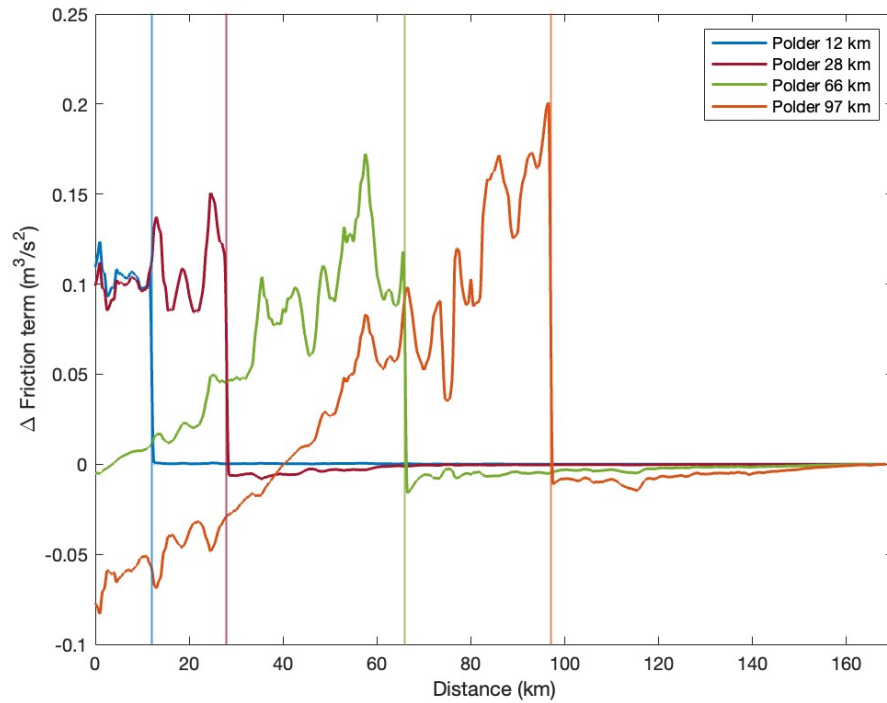
C | Model results

Figure C.1: Change in the Friction term of the momentum equation (Equation 3.5) for model runs with an added intertidal area at different locations. The vertical lines show the location of the intertidal area along the channel.
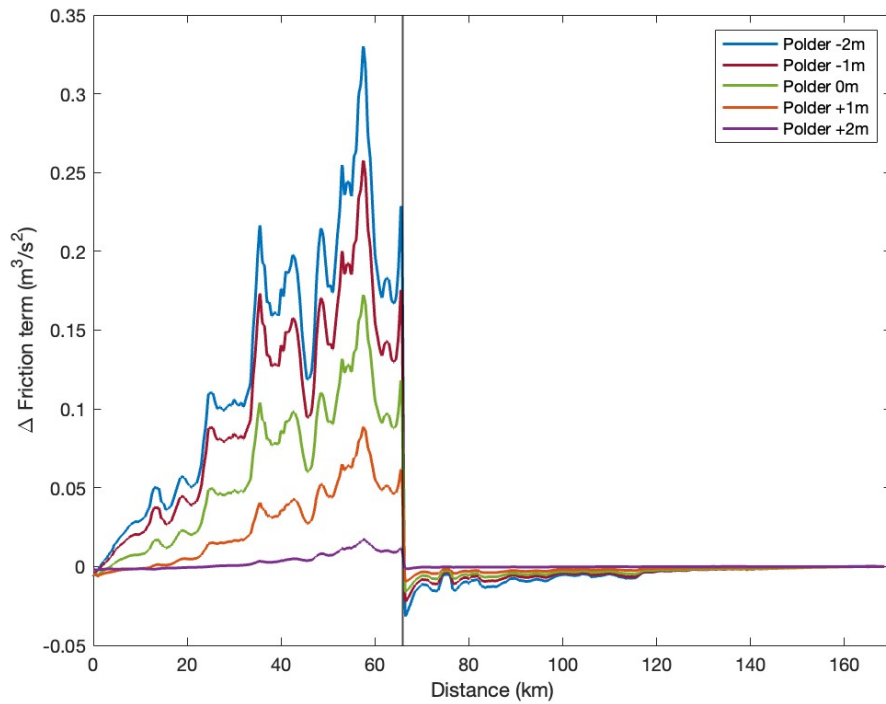
Figure C.2: Change in the Friction term of the momentum equation (Equation 3.5) for model runs with an added intertidal area at 66 km from the mouth for different elevations. The vertical line shows the location of the implemented intertidal area along the channel.
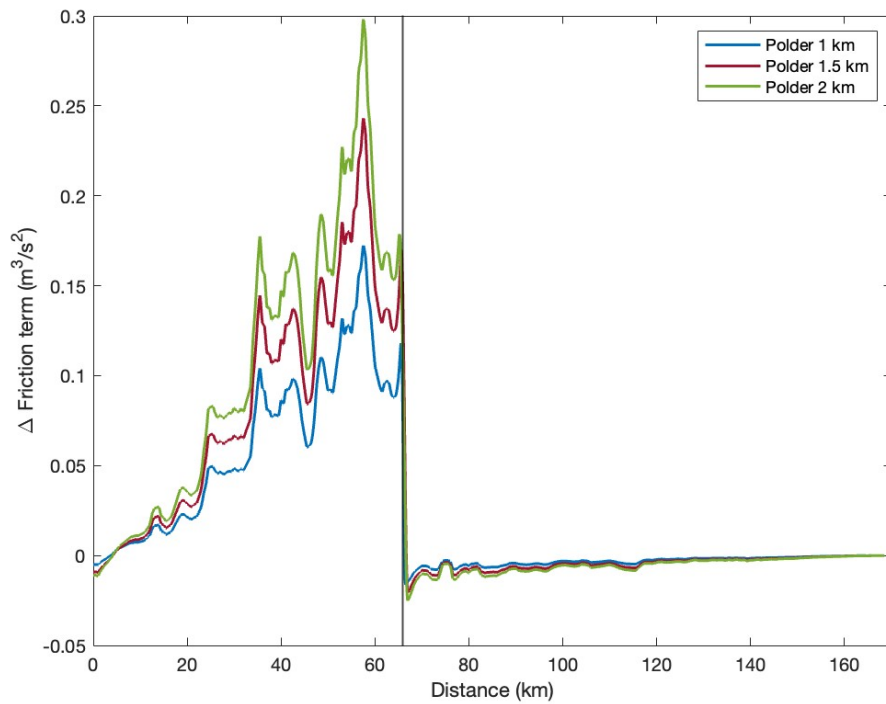

Figure C.3: Change in the Friction term of the momentum equation (Equation 3.5) for model runs with an added intertidal area of different widths parallel to the channel. The vertical line shows the location of the intertidal area along the channel.